Title

NPC1 regulates the distribution of phosphatidylinositol 4-kinases at Golgi and lysosomal membranes

Journal

The EMBO Journal, 40(13)

ISSN

0261-4189

Authors

Kutchukian, Candice

Vivas, Oscar

Casas, Maria

et al.

Publication Date

2021-07-01

DOI

10.15252/embj.2020105990

Article

SOURCE DATA | TRANSPARENT PROCESS | OPEN ACCESS

THE EMBO JOURNAL

NPC1 regulates the distribution of phosphatidylinositol 4-kinases at Golgi and lysosomal membranes

Candice Kutchukian[1,†], Oscar Vivas[1,†,‡], Maria Casas[1], Julia G Jones[1], Scott A Tiscione[1], Sergi Simó[2], Daniel S Ory[3], Rose E Dixon[1] & Eamonn J Dickson[1,*]

Abstract

Cholesterol and phosphoinositides (PI) are two critically important lipids that are found in cellular membranes and dysregulated in many disorders. Therefore, uncovering molecular pathways connecting these essential lipids may offer new therapeutic insights. We report that loss of function of lysosomal Niemann-Pick Type C1 (NPC1) cholesterol transporter, which leads to neurodegenerative NPC disease, initiates a signaling cascade that alters the cholesterol/phosphatidylinositol 4-phosphate (PtdIns4P) countertransport cycle between Golgi-endoplasmic reticulum (ER), as well as lysosome-ER membrane contact sites (MCS). Central to these disruptions is increased recruitment of phosphatidylinositol 4-kinases—PI4KIIα and PI4KIIIβ—which boosts PtdIns4P metabolism at Golgi and lysosomal membranes. Aberrantly increased PtdIns4P levels elevate constitutive anterograde secretion from the Golgi complex, and mTORC1 recruitment to lysosomes. NPC1 disease mutations phenocopy the transporter loss of function and can be rescued by inhibition or knockdown of either key phosphoinositide enzymes or their recruiting partners. In summary, we show that the lysosomal NPC1 cholesterol transporter tunes the molecular content of Golgi and lysosome MCS to regulate intracellular trafficking and growth signaling in health and disease.

Keywords membrane contact sites; mTORC; neurodegeneration; Niemann-Pick Type C; phosphoinositides

Subject Categories Membranes & Trafficking; Organelles

DOI 10.15252/embj.2020105990 | Received 22 June 2020 | Revised 11 March 2021 | Accepted 19 March 2021 | Published online 21 May 2021

The EMBO Journal (2021) 40: e105990

Introduction

Phosphoinositides are a family of eight phospholipids that define membrane identity by transducing extracellular signals, controlling ion channel function, facilitating cell movement, and orchestrating intracellular trafficking (reviewed, (De Matteis & Godi, 2004; Balla, 2013; Hille *et al*, 2015; Dickson & Hille, 2019). Given their importance in coordinating these fundamental cellular events, it is perhaps not surprising that disease mutations or changes in expression of phosphoinositide metabolizing enzymes have been implicated in viral replication (Bishe *et al*, 2012; Sasaki *et al*, 2012; McPhail *et al*, 2019), devastating developmental disorders (Staiano *et al*, 2015), cancer (Bunney & Katan, 2010; Thapa *et al*, 2016; Fruman *et al*, 2017; Waugh, 2019), and neurodegenerative diseases (Leissring *et al*, 1999; Staiano *et al*, 2015; Vivas *et al*, 2019). Thus, understanding mechanisms that regulate and control phosphoinositides is essential from both a cell biological and clinical perspective.

At the Golgi complex, a single mono-phosphorylated species called phosphatidylinositol 4-phosphate (PtdIns4P) predominates and is required for regulated Golgi vesicular trafficking events, signaling and metabolic function, and structural integrity. Golgi PtdIns4P is synthesized by the ATP-dependent phosphorylation of phosphatidylinositol (PtdIns) by Golgi-targeted lipid kinases, termed phosphatidylinositol 4-kinases (PI4K). Four different PI 4-kinases are expressed in most human cells; the type I PI 4-kinase IIIα (PI4KIIIα) and PI 4-kinase IIIβ (PI4KIIIβ) enzymes and the structurally distinct type II PI 4-kinases, PI4KIIα and PI4KIIβ (Balla & Balla, 2006). At the Golgi complex, the PI4KIIIβ and PI4KIIα isoforms are the major enzymes responsible for regulating Golgi PtdIns4P-dependent events. Dysregulation of Golgi PtdIns4P metabolism and the PtdIns4P protein interactome features in many cancers and is often associated with tumor progression (Waugh, 2019). Despite evidence linking altered PtdIns4P in cancers, information regarding dysfunctional PtdIns4P metabolism in neurodegenerative diseases is lacking.

In addition to *de novo* lipid synthesis, target organelle membranes can have lipids transported to them from donor membranes. This form of lipid transport occurs at regions where organelle membranes are less than 20 nm apart, termed membranes contact sites (MCS), and is facilitated by lipid transfer proteins. At

1 Department of Physiology and Membrane Biology, University of California, Davis, CA, USA
2 Department of Cell Biology & Human Anatomy, University of California, Davis, CA, USA
3 Department of Internal Medicine, Washington University School of Medicine, St. Louis, MO, USA
*Corresponding author. Tel: +1 530 752 6195; E-mail: ejdickson@ucdavis.edu
†These authors contributed equally to this work
‡Present address: Department of Physiology and Biophysics, University of Washington, Seattle, WA, USA

MCS between trans-Golgi network (TGN) and endoplasmic reticulum (ER) (Mesmin *et al*, 2013), or between the lysosome and ER (Lim *et al*, 2019), oxysterol-binding protein (OSBP) mediates the transport of PtdIns4P down its concentration gradient to the ER, fueling the countertransport cycle of cholesterol against its steep concentration gradient (Mesmin *et al*, 2013). This cholesterol/PtdIns4P exchange contributes to the establishment of a cholesterol gradient between organelles of the secretory pathway and is essential for protein trafficking to the plasma membrane (PM) (Péresse *et al*, 2020) and mTORC1 recruitment to lysosomes (Lim *et al*, 2019). At ER-TGN MCS, PI4KIIα and PI4KIIIβ, as well as an ER PtdIns4P phosphatase (SAC1), maintain the TGN PtdIns4P gradient to perpetuate this exchange cycle (Mesmin *et al*, 2013; Zewe *et al*, 2018; Mesmin *et al*, 2019; Venditti *et al*, 2019). Likewise, SAC1 and OSBP have also been identified as being essential for cholesterol/PtdIns4P exchange at ER-lysosome MCS. Despite this knowledge, essential information is still unknown, such as (i) the molecular identity of the PI4K that generates PtdIns4P for ER-lysosome lipid transport and (ii) if this molecular choreography is disrupted during pathophysiological conditions.

Here, we report that in Niemann-Pick Type C1 (NPC1) disease, a pathological neurodegenerative disorder of altered cholesterol homeostasis, there is a rearrangement of molecular components of the cholesterol/PtdIns4P cycle. Specifically, we demonstrate that disease mutations or loss of lysosomal NPC1 function leads to the aberrant accumulation of PtdIns4P on Golgi and lysosomal membranes. Underlying altered distribution of PtdIns4P is cholesterol-dependent transcriptional changes in the recruitment machinery of PI4K metabolizing enzymes. Consequences of altered Golgi and lysosomal PtdIns4P are enhanced anterograde trafficking to the PM and mTORC1 recruitment to lysosomes, respectively. We propose that the lysosomal NPC1 cholesterol transporter tunes the molecular elements of both ER-TGN and ER-lysosome MCS in health and disease to regulate trafficking and growth signaling.

Results

Loss of NPC1 function leads to increased Golgi and lysosomal PtdIns4P levels

Niemann-Pick Type C1 (NPC1) is a lysosomal cholesterol transporter that facilitates the egress of cholesterol across the lysosome lumen to other cellular membranes. Inhibition, loss of function, or disease mutations in NPC1 cause the accumulation of lysosomal cholesterol and altered cellular cholesterol homeostasis (Appendix Fig S1A–C). Given the interdependent relationship between cholesterol and PtdIns4P levels at MCS (Antonny *et al*, 2018; Mesmin *et al*, 2019), we hypothesized that loss of NPC1 function may lead to changes in cellular PtdIns4P levels. To test this hypothesis, we quantified changes in the distribution of the PtdIns4P biosensor P4M (Hammond *et al*, 2014) under three different NPC1 conditions: inhibition, knockout, and disease mutations. Inhibition of NPC1 using the specific inhibitor U18666A (Lu *et al*, 2015) (U18) resulted in the significant accumulation of P4M at perinuclear and endolysosomal regions in tsA201 cells (Fig 1A and B) and neurons (Fig 1C and D). To confirm that U18-mediated increases in cellular PtdIns4P were not due to some off-target effect of the U18 compound, we analyzed the distribution of the P4M biosensor in NPC1$^{-/-}$ cells. Similar to pharmacological inhibition of NPC1, its genetic knockout also resulted in similar PtdIns4P accumulation (Appendix Fig S1D and E). Finally, to determine if elevated PtdIns4P levels are a cellular phenotype of NPC disease, we expressed the P4M biosensor in patient fibroblasts that harbor the most common NPC1 mutation (NPC1^{I1061T}). Similar to U18-treated and NPC1$^{-/-}$, NPC1^{I1061T} patient fibroblasts had significantly increased PtdIns4P levels in perinuclear and endolysosomal regions (Appendix Fig S1F and G). To characterize the subcellular localization of PtdIns4P, we coexpressed P4M with either *trans*-Golgi network (TGN38-CFP) or lysosomal (LAMP1-RFP) markers in patient fibroblasts. Quantitative analyses revealed that PtdIns4P significantly increased at both TGN (Fig 1E–G) and lysosome membranes (Fig 1H–J and Appendix Fig S1H–J). Increases in Golgi PtdIns4P occurred independently of changes in gross Golgi structure as super-res imaging (resolution ~ 120 nm) of Giantin and TGN46 revealed no significant differences in TGN area from fibroblasts or U18-treated cells (Appendix Fig S1K–M).

To endorse P4M biosensor data, we also quantitatively analyzed phosphoinositide levels across different brain regions of a NPC1^{I1061T} murine model that faithfully recapitulates the most common phenotypes of the human disease (Praggastis *et al*, 2015). Mass spectrometry lipid analysis of the phosphoinositide composition from four different NPC1^{I1061T} brain regions (mid-brain, hippocampus, cortex, and cerebellum) confirmed significant

Figure 1. PtdIns4P accumulates in Golgi and lysosomal compartments following loss of NPC1 function.

A Confocal images of live control (top) and U18-treated (bottom) tsA201 cells expressing P4M-YFP. Black and orange rectangles show expanded views of PtdIns4P in perinuclear and endo/lysosomal compartments, respectively.
B Quantification of perinuclear P4M-YFP mean fluorescence intensity normalized to the cytoplasm. Control: $n = 19$; U18: $n = 16$.
C Confocal images of control and U18-treated hippocampal neurons transfected with P4M-YFP. The inset panels show expanded views of PtdIns4P in perinuclear regions.
D Quantification of perinuclear P4M-YFP mean fluorescence intensity normalized to the cytoplasm. Control: $n = 11$; U18: $n = 10$.
E Control (top) and NPC1^{I1061T} (bottom) patient fibroblasts transfected with P4M-YFP (left), TGN38-CFP, and merge (right). Black rectangles show expanded views of PtdIns4P in TGN38 regions. Dashed white lines were used for intensity profile analysis (F).
F Line scan analysis taken from white dashed lines in (E) showing intensity changes of P4M and TGN38 signal from control (top) and NPC1^{I1061T} (bottom) cells.
G Quantification of P4M signal in TGN38 region (P4M$_{TGN38}$). Control: $n = 12$; NPC1^{I1061T}: $n = 19$.
H Same as (E) only LAMP1-RFP expressed instead of TGN38.
I Same as (F) only LAMP1 instead of TGN38.
J Quantification of P4M signal in LAMP1 regions (P4M$_{LAMP1}$). Control: $n = 14$; NPC1^{I1061T}: $n = 16$.
K Heat map of PtdIns, PtdIns*P* and PtdInsP_2 levels from 4 different murine brain regions. The colors from green to red indicate the relative contents of lipid isoforms in different brain regions from NPC1^{I1061T} mice relative to wild-type brains; $n = 3$ for both WT and NPC1^{I1061T} animals.

Data information: Data are all expressed as mean ± SEM from individual cells. *$P < 0.05$; **$P < 0.01$; ****$P < 0.0001$ with unpaired *t*-test.
Source data are available online for this figure.

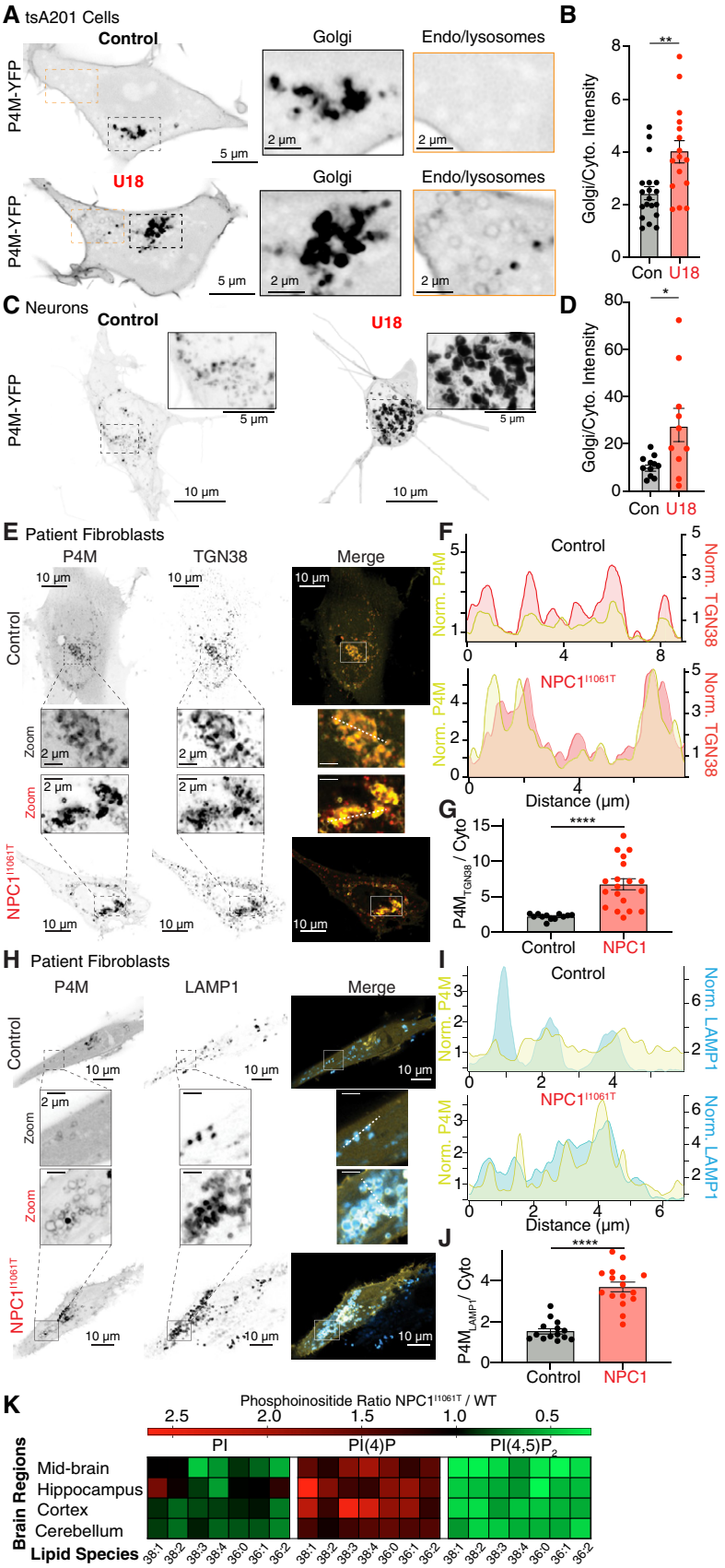
A tsA201 Cells
Control
U18
P4M-YFP
Golgi
Endo/lysosomes
5 µm
2 µm
B
Golgi/Cyto. Intensity
Con
U18
C Neurons
D
E Patient Fibroblasts
P4M
TGN38
Merge
Zoom
NPC1I1061T
F
Norm. P4M
Norm. TGN38
Distance (µm)
G
P4MTGN38 / Cyto
Control
NPC1
H Patient Fibroblasts
LAMP1
I
Norm. LAMP1
J
P4MLAMP1 / Cyto
K
Phosphoinositide Ratio NPC1I1061T / WT
PI
PI(4)P
PI(4,5)P2
Brain Regions
Mid-brain
Hippocampus
Cortex
Cerebellum
Lipid Species

Figure 1.

elevations in global PtdInsP levels relative to wild-type age and sex-matched littermates (Fig 1K). Consistent with NPC1 global brain expression, the increase of PtdInsP in NPC1^{I1061T} brains was not region-specific, with PtdInsP levels significantly elevated across each area, suggesting that the loss of NPC1 function alters the levels of PtdInsP regardless of region. Furthermore, increases in PtdInsP were paralleled by decreases in PtdIns and PtdInsP_2 (Vivas *et al*, 2019), confirming broader control of phosphoinositide species by NPC1. Collectively, these data support a link between the lysosome NPC1 protein and regulation of Golgi and Lysosome PtdIns4P levels.

NPC1 regulates the molecular elements of ER-TGN membrane contact sites

At ER-TGN and ER-Lysosome MCS, OSBP (Mesmin *et al*, 2013; Lim *et al*, 2019), VAPA (Peretti *et al*, 2008; Lim *et al*, 2019), and SAC1 (Zewe *et al*, 2018; Lim *et al*, 2019) serve as important regulators of PtdIns4P homeostasis (Fig 2A). Thus, we tested if loss of NPC1 function can tune the expression and localization of ER-TGN MCS proteins to potentially account for the changes in subcellular PtdIns4P distribution.

Western blot analysis from U18-treated cells revealed that total cellular protein levels of OSBP were not significantly different from control cells (Fig 2B). Subsequent super-resolution immunofluorescence analysis from tsA201 cells treated with U18 revealed that although cellular protein levels were similar, significantly more OSBP localized to TGN46 regions (Fig 2C and D). Similar results were obtained from NPC1^{I1061T} patient cells (Fig EV1A and B) and U18-treated neurons (Fig 2E and F) compared to appropriate controls. OSBP is recruited to ER-TGN junctions through dual interactions of its PH domain with Golgi PtdIns4P and binding of its FFAT motif to the type II ER membrane protein VAPA (Levine & Munro, 2002; Loewen *et al*, 2003). With this in mind, we asked if VAPA also accumulates in Golgi regions of cells lacking NPC1? Immunofluorescence analysis determined that, similar to OSBP, VAPA accumulated at the TGN in U18-treated tsA201 cells (Fig 2G and H), at the Golgi of NPC1^{I1061T} patient cells (Fig EV1C and D), and perinuclear regions of NPC1$^{-/-}$ cells (Fig EV1E and F).

Parallel increases in PtdIns4P (Fig 1), OSBP (Fig 2C–F), and VAPA (Fig 2G and H) at ER-TGN MCS have been observed under circumstances of OSBP inhibition (Mesmin *et al*, 2017). Therefore, we tested if OSBP-mediated PtdIns4P transport kinetics are altered following loss of NPC1 function. To test this hypothesis, we first transfected tsA201 cells with GFP-P4M, to monitor TGN PtdIns4P, and transiently treated cells with a specific inhibitor of PI4KIIIβ activity (PIK93 (Toth *et al*, 2006)). PI4KIIIβ is responsible for local PtdIns4P production in the vicinity of OSBP (Mesmin *et al*, 2017); thus, inhibiting PI4KIIIβ, while monitoring P4M intensity at the TGN, allows us to indirectly track the rate of PtdIns4P molecules consumed by OSBP. Transient application of PIK93 caused a rapid and reversible drop in P4M intensity at the Golgi from both control and U18-treated tsA201 cells (Fig EV1G and H). Comparison of vehicle and U18-treated cells revealed that loss of NPC1 function results in both a significantly larger and faster loss of PtdIns4P. This decrease in PtdIns4P biosensor intensity may represent PtdIns4P transferred from the TGN to the ER where it is subsequently degraded by the ER lipid phosphatase SAC1. To more directly measure OSBP kinetics following loss of NPC1 function, we also transfected tsA201 cells with GFP-P4M and treated with a selective OSBP inhibitor (OSW-1 (Burgett *et al*, 2011)). Time series analysis revealed that loss of OSBP function resulted in faster recruitment of GFP-P4M to the TGN compared to vehicle controls (Fig EV1I and J). Together, these data provide evidence that OSBP-mediated transport of PtdIns4P is accelerated and therefore unlikely to be directly facilitating increases in PtdIns4P following NPC1 loss of function.

Maintenance of the OSBP transfer cycle requires a steep PtdIns4P gradient to be conserved across ER-TGN MCS. This chemical gradient is conserved through the enzymatic actions of SAC1, which degrades its PtdIns4P substrate on ER membranes (Fig 2A). In light of increased TGN PtdIns4P, VAPA, and OSBP levels in cells lacking functional NPC1 (Figs 1 and 2C–H), we asked if SAC1 at ER-TGN MCS is also sensitive to changes in NPC1 function. Measurement of SAC1 protein levels revealed no significant difference between control and NPC1^{I1061T} patient cells (Fig 2I). Overnight inhibition of NPC1 in GFP11-SAC1 cells (endogenous SAC1 tagged with a GFP (Zewe *et al*, 2018)) caused a significant redistribution of SAC1 to

Figure 2. NPC1 regulates the contents of ER-TGN membrane contact sites.

A Diagram of the molecular elements within ER-TGN membrane contact sites.
B Representative Western blot for OSBP in control and U18-treated tsA201 cells. Protein levels were determined by densitometry with β-actin normalization. Each point ($n = 3$) represents protein levels from U18-treated cells normalized to control bands.
C Confocal images of control and U18-treated tsA201 cells fixed and stained for OSBP (left), TGN46 (middle), and merge (right). Black rectangles show expanded views of OSBP and TGN46 regions.
D Quantification of OSBP signal in TGN46 regions ($OSBP_{TGN46}$). Control: $n = 40$; U18: $n = 39$.
E Confocal images of control and U18-treated hippocampal neurons fixed and stained for OSBP. Dashed black lines represent the outline of each neuron.
F Quantification of OSBP in perinuclear region of control and U18-treated neurons. Control: $n = 10$; U18: $n = 14$.
G Confocal images of control and U18-treated tsA201 cells fixed and stained for VAPA (left), TGN46 (middle), and merge (right). Black rectangles show expanded views of VAPA and TGN46 regions.
H Quantification of VAPA signal in TGN46 regions ($VAPA_{TGN46}$). Control: $n = 44$; U18: $n = 44$.
I Representative Western blot of SAC1 in control and U18-treated tsA201 cells. Protein levels were normalized to β-actin, $n = 4$.
J Confocal images of control and U18-treated GFP11-SAC1 HEK293 cells (top) and control and NPC1^{I1061T} patient fibroblasts immunolabeled with anti-SAC1 antibody (bottom). Insets show an enlarged view of SAC1 centered on a perinuclear region.
K Quantification analyses of GFP11-SAC1 (top; Control: $n = 10$; U18: $n = 10$) and anti-SAC1 (bottom; Control: $n = 7$; NPC1^{I1061T}: $n = 8$) mean fluorescence intensities in Golgi normalized to the cytoplasm.

Data information: Data are all expressed as mean ± SEM from individual cells, and all statistical analyses were conducted using unpaired *t*-test with $*P < 0.05$; $**P < 0.01$; $***P < 0.001$; and $****P < 0.0001$.
Source data are available online for this figure.

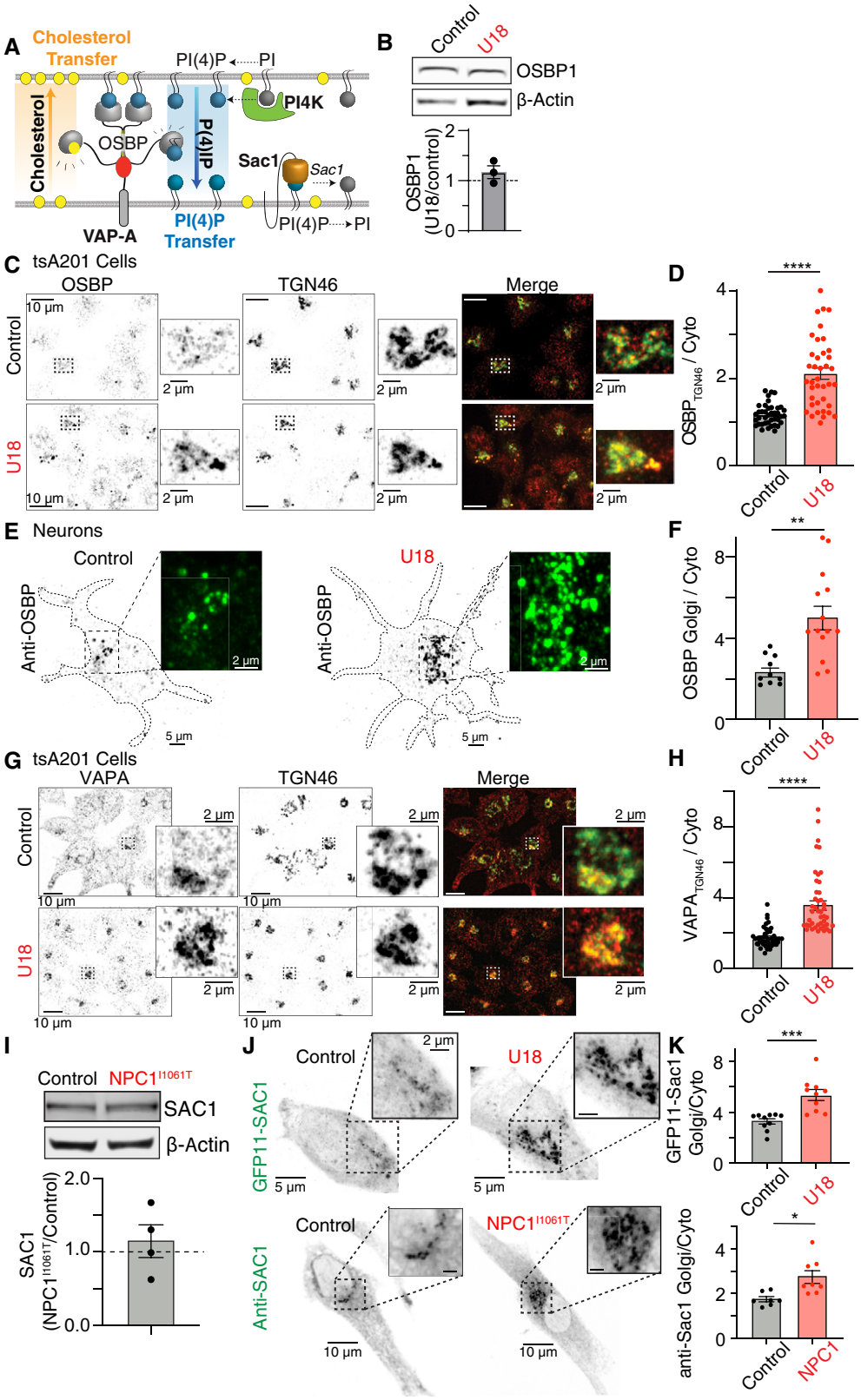
A
Cholesterol Transfer
PI(4)P
PI
PI4K
Cholesterol
OSBP
P(4)P
Sac1
Sac1
VAP-A
PI(4)P Transfer
PI(4)P
PI
B
Control
U18
OSBP1
β-Actin
OSBP1 (U18/control)
C tsA201 Cells
OSBP
TGN46
Merge
Control
U18
10 μm
2 μm
D
OSBP TGN46 / Cyto
****
Control
U18
E Neurons
Control
U18
Anti-OSBP
2 μm
5 μm
F
OSBP Golgi / Cyto
**
G tsA201 Cells
VAPA
TGN46
Merge
H
VAPA TGN46 / Cyto
****
I
Control
NPC1I1061T
SAC1
β-Actin
SAC1 (NPC1I1061T/Control)
J
Control
U18
GFP11-SAC1
5 μm
Anti-SAC1
NPC1I1061T
10 μm
K
GFP11-Sac1 Golgi/Cyto
***
anti-Sac1 Golgi/Cyto
*
NPC1

Figure 2.

Golgi regions (Fig 2J–K). This result is underscored by immunofluorescence analysis of endogenous SAC1 in $NPC1^{I1061T}$ patient cells that revealed a similar accumulation of SAC1 at Golgi regions (Fig 2J and K; Appendix Fig S2A–C). SAC1's precise localization at ER-TGN regions is controversial with some groups offering evidence for SAC1 being localized in ER membranes and acting in cis (Mesmin & Bigay, 2013; Zewe *et al*, 2018) or trans (Venditti *et al*, 2019) to dephosphorylate TGN PtdIns4P, while others have proposed SAC1 can traffic to Golgi membranes under different growth conditions to regulate Golgi PtdIns4P levels (Blagoveshchenskaya *et al*, 2008). Using super-resolution microscopy, we quantified the relative distribution of endogenous SAC1 at the ER and TGN from live vehicle control or U18-treated HEK cells. Appendix Fig S2A–C demonstrates that inhibition of NPC1 leads to an increase in SAC1 at TGN46-positive regions ($SAC1_{TGN46}$) that occurs in the absence of any changes to SAC1 at SEC61β-positive regions ($SAC1_{SEC61\beta}$). To further examine if loss of NPC1 function can alter the gross distribution of ER and TGN, we immunostained GFP11-SEC61β HEK cells (Zewe *et al*, 2018) and COS7 cells (expressing mCherry-SEC61β) for TGN46. Analysis of SEC61β and TGN38 fluorescent signals revealed no significant changes in overlapping pixels or TGN area following U18 treatment (Appendix Fig S2D–G). Thus, at this resolution (~ 120 nm), given no clear alterations in ER-TGN distribution, we suggest it is the redistribution of SAC1 to ER-TGN MCS, rather than gross changes to ER-MCS architecture that underlies increases in SAC1. In addition to redistribution of SAC1 at ER-TGN MCS, we also observed increased recruitment of SAC1 at ER-Lysosome MCS (Appendix Fig S2H–J), supporting a role for SAC1 in maintaining the step PtdIns4P gradient between ER and other membranes. Collectively, these data demonstrate that NPC1 has the ability to influence elements within ER-TGN MCS but does not provide a direct explanation as to why TGN PtdIns4P levels are increased in NPC1 disease.

Inhibition or disease mutations in NPC1 recruit PI4K enzymes to Golgi and Lysosome membranes

Given that NPC1-mediated changes in VAPA, OSBP, and SAC1 distribution are likely positioned downstream of increases in PtdIns4P levels, we next asked if loss of NPC1 function more directly influences PtdIns4P-metabolizing enzymes. Cellular PtdIns4P levels are controlled in space and time through the enzymatic activities of the PI4K family of enzymes (PI4KIIα, PI4KIIβ, PI4KIIIα, PI4KIIIβ; Fig 3A). Increases in catalytic activity and/or membrane localization of PI4K lipid enzymes would represent the most intuitive route to increase PtdIns4P levels through the phosphorylation of phosphatidylinositol (PtdIns; Fig 3A). Of the four PI4K family members, PI4KIIα and PI4KIIIβ have been demonstrated to localize to Golgi and lysosome membranes at steady state (Weixel *et al*, 2005; Sridhar *et al*, 2013). To assess if a simple increase in the abundance of these PI4K enzymes is responsible for elevated PtdIns4P levels, cell lysates from U18-treated tsA201 cells were immunoblotted for PI4KIIα and PI4KIIIβ (Fig 3B). Western blot analysis determined no changes in the total cellular protein expression of either PI4KIIα or PI4KIIIβ enzymes, suggesting that a simple increase in protein amount is unlikely to account for the elevated TGN and lysosomal PtdIns4P levels.

Next, we tested the hypothesis that increased recruitment of PI4K enzymes may underlie the elevations in Golgi or Lysosome PtdIns4P levels following NPC1 inhibition, knockout, or mutation. To this end, we expressed fluorescently tagged PI4K enzymes and quantified their cellular distribution in NPC1 patient cells, U18-treated tsA201 cells, and neurons. PI4KIIβ and PI4KIIIα had a similar subcellular distribution across control and U18-treated tsA201 cells (Appendix Fig S3A and B) and thus were excluded from further analysis. In contrast, quantification of overexpressed PI4KIIα and PI4KIIIβ revealed significantly increased levels of both enzymes at perinuclear regions in U18-treated tsA201 cells relative to control (Fig 3C and D). To more precisely determine if these perinuclear increases in enzyme localization reflect increases at the TGN, we fixed control and U18-treated tsA201 cells before staining for endogenous PI4KIIα and PI4KIIIβ levels and TGN46. Super-resolution imaging analysis revealed that the fraction of PI4KIIα (Fig 3E and F) and PI4KIIIβ (Fig 3G and H) overlapping with TGN46 significantly increased following loss of NPC1 function. Similar results were observed with a second more general Golgi marker; Giantin (Appendix Fig S4A–D). These observations were also consistent for neurons (Fig 3I and J), $NPC1^{-/-}$ cells (Appendix Fig S3G–J), and $NPC1^{I1061T}$ patient fibroblasts (Appendix Figs S3C–F and S4E–L).

In addition to increased PI4KIIα and PI4KIIIβ levels at Golgi membranes, we also observed that fluorescently tagged PI4KIIα and PI4KIIIβ preferentially localized to endolysosomal locations in $NPC1^{I1061T}$ patient cells (Fig EV2A–D). This distribution is consistent with increased lysosomal PtdIns4P observed following loss of

Figure 3. PI4KIIα and PI4KIIIβ are recruited to Golgi and lysosome membranes in NPC1 disease.

A Diagram showing PtdIns4P metabolizing enzymes.

B Representative Western blot for PI4KIIα and PI4KIIIβ in control and U18-treated tsA201 cells. Protein levels were normalized to β-actin. Individual points (PI4KIIα: $n = 3$; PI4KIIIβ: $n = 4$) represent protein levels of each +U18 band normalized to control.

C Left: Confocal images of control (left) and U18-treated (right) tsA201 cells expressing PI4KIIα-GFP. Bottom panels show an enlarged view of the probe centered on a perinuclear region. Right: Quantification of perinuclear PI4KIIα intensity relative to the cytoplasm. Control: $n = 12$; U18: $n = 14$.

D Same as (C) only PI4KIIIβ. Control: $n = 12$; U18: $n = 15$.

E Confocal images of control and U18-treated tsA201 cells fixed and stained for PI4KIIα (left), TGN46 (middle), and merge (right). Black rectangles show expanded views of PI4KIIα and TGN46 regions.

F Quantification of PI4KIIα signal in TGN46 regions ($PI4KII\alpha_{TGN46}$). Control: $n = 36$; U18: $n = 36$.

G, H same as (E, F) only stained with PI4KIIIβ. Control: $n = 35$; U18: $n = 43$.

I, J same as (C, D) except using hippocampal neurons. (I) Control: $n = 7$; U18: $n = 8$. (J) Control: $n = 6$; U18: $n = 6$.

Data information: Data are all expressed as mean ± SEM from individual cells, and all statistical analyses were conducted using unpaired *t*-test with $^{**}P < 0.01$; $^{***}P < 0.001$; $^{****}P < 0.0001$.
Source data are available online for this figure.

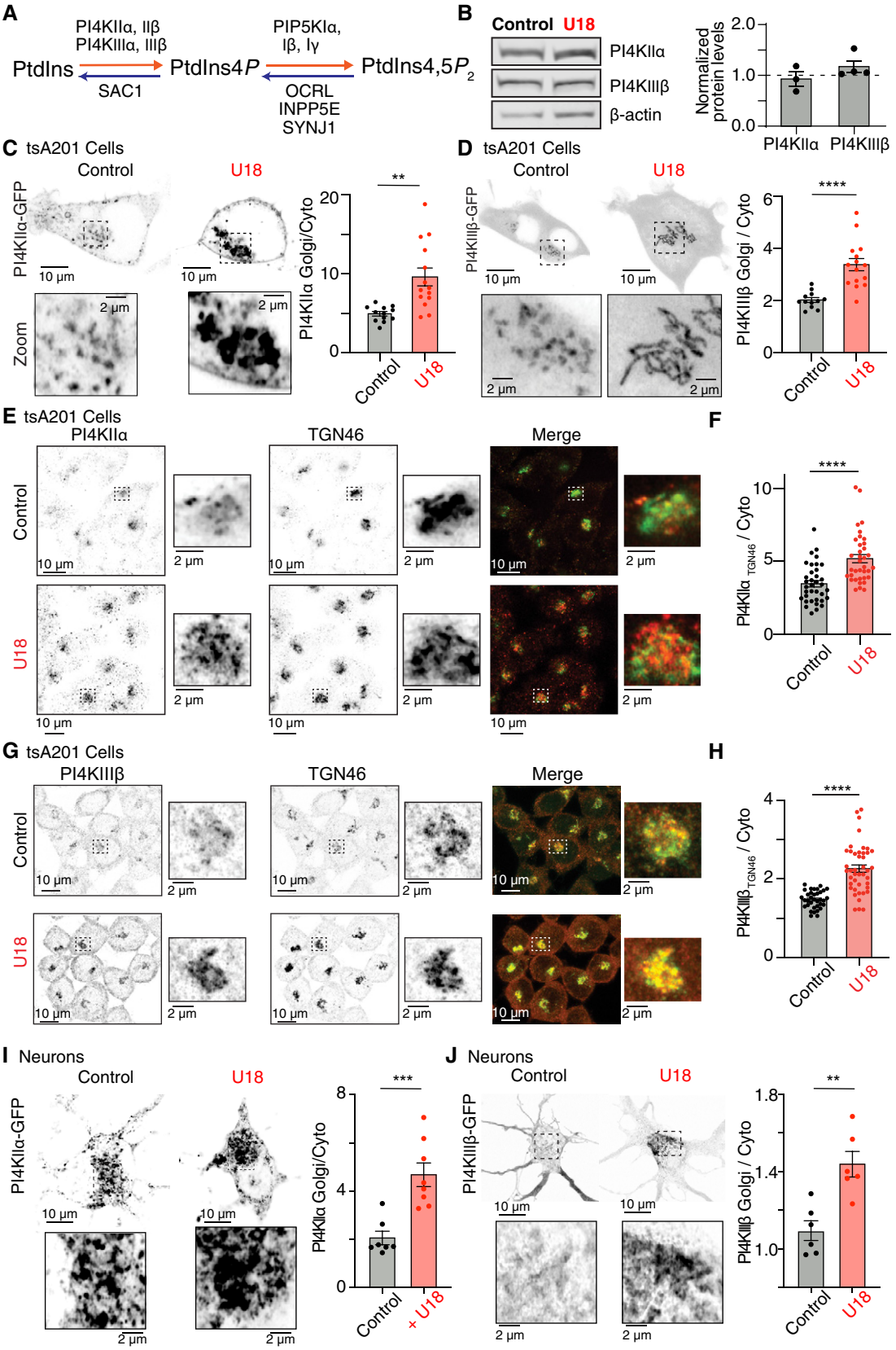
A
PI4KIIα, IIβ
PI4KIIIα, IIIβ
PtdIns
PtdIns4P
PtdIns4,5P2
SAC1
PIP5KIα,
Iβ, Iγ
OCRL
INPP5E
SYNJ1
B
Control U18
PI4KIIα
PI4KIIIβ
β-actin
Normalized protein levels
PI4KIIα PI4KIIIβ
C tsA201 Cells
Control
U18
PI4KIIα-GFP
Zoom
PI4KIIα Golgi/Cyto
D tsA201 Cells
PI4KIIIβ-GFP
PI4KIIIβ Golgi / Cyto
E tsA201 Cells
PI4KIIα
TGN46
Merge
F
PI4KIIα TGN46 / Cyto
G tsA201 Cells
PI4KIIIβ
H
PI4KIIIβ TGN46 / Cyto
I Neurons
J Neurons
10 µm
2 µm
**
***
****

Figure 3.

NPC1 function (Fig 1H–J). In line with the concept that PI4KIIα and PI4KIIIβ are responsible for elevations in lysosomal PtdIns4P in NPC1 disease, endogenous levels of both enzymes were significantly elevated at LAMP1-positive membranes (Fig EV2E–H). These data suggest a NPC1-dependent mechanism, conserved across multiple cells types, for the recruitment of PI4KIIα and PI4KIIIβ to Golgi and lysosome membranes.

DHHC3-dependent recruitment of PI4KIIα underlies NPC1-dependent increases in Golgi PtdIns4P

Localization of PI4K isoforms can be influenced by a number of factors including palmitoylation (Lu *et al*, 2012), phosphorylation (Hausser *et al*, 2005), and protein interactions (Haynes *et al*, 2005; Sasaki *et al*, 2012; Greninger *et al*, 2013; Chalupska *et al*, 2019). For PI4KIIα, the lipid kinase activity, Golgi localization, and membrane binding are dependent on the palmitoylation of a cysteine-rich motif by DHHC3 and DHHC7 palmitoyl acyltransferases (Asp-His-His-Cys; DHHC; (Fig 4A)) (Lu *et al*, 2012). To confirm a central role for PI4KIIα in increasing subcellular PtdIns4P levels following NPC1 loss of function, we first decided to knockdown PI4KIIα levels. To this end, we transfected Cas9-expressing HEK293 cells for 48 h with sgPI4KIIα and a fluorescent transfection marker. Western blot analysis revealed that total PI4KIIα protein was reduced by ~ 75%, a reduction mirrored by immunofluorescence analysis from randomized regions of interest (Fig EV3A and B). A targeted analysis of only those cells transfected with a fluorescent marker revealed a significantly larger, ~ 90% reduction in immunofluorescence signal at Golgi regions (Fig EV3C). Based on these analyses, all subsequent quantifications were performed on cells positive for a transfection marker.

To test if reducing PI4KIIα protein levels affected NPC1-dependent increases in PtdIns4P, we quantified the cellular distribution of P4M-YFP (Fig 4B and C). Comparing control, U18-treated, and U18-treated PI4KIIα knockdown ("sgPI4KIIα") cells revealed that sgPI4KIIα significantly reduced steady-state and U18-dependent increases in Golgi PtdIns4P (Fig 4B and C). To establish a role for DHHC3 in recruiting PI4KIIα to the Golgi, we quantified the distribution of endogenous DHHC3 in control and $NPC1^{I1061T}$ patient fibroblasts. Analysis of immunofluorescent images revealed $NPC1^{I1061T}$ fibroblasts had significantly elevated DHHC3 at Golgi regions (Fig 4D and E). In contrast to endogenous DHHC3, the expression of HA-DHHC7 was not significantly different between control and $NPC1^{I1061T}$ patient cells (Fig EV3D) and was not further investigated. These data suggest that an increase in PI4KIIα palmitoylation may underlie increases in PtdIns4P following loss of NPC1 function. To test this hypothesis further, we overexpressed DHHC3 in control fibroblasts to determine if simply increasing DHHC3 levels resulted in changes to P4M and PI4KIIα at Golgi membranes. Quantitative analyses revealed that overexpressing DHHC3 in control cells resulted in an increase in both P4M (Fig 4F and G) and PI4KIIα (Fig 4H and I), but not PI4KIIIβ, at Golgi membranes to a similar range as NPC1 cells. Thus, transiently overexpressing DHHC3 increases Golgi PtdIns4P to a similar level as NPC loss of function cells. To further test a role for DHHC3 in recruiting PI4KIIα to Golgi membranes, we knocked down DHHC3 by ~ 90% ("sgDHHC3"; Fig EV3E) using CRISPR-Cas9 editing and found that reducing DHHC3 levels in NPC1 loss of function cells normalized PtdIns4P back into a control range (Fig 4J; analysis Fig 4C). To rule out off-target effects of CRISPR editing or alterations in Golgi integrity due to DHHC3 knockdown, we expressed a dominant-negative $DHHC3^{C157S}$ plasmid (DN-DHHC3 (Lu *et al*, 2012)), that lacks the

Figure 4. NPC1 loss of function increases DHHC3-mediated PI4KIIα recruitment and PtdIns4P on Golgi and lysosome membranes.

A Diagram illustrating the Golgi recruitment mechanisms of PI4KIIα.
B Confocal images of wild-type and PI4KIIα-depleted (sgPI4K2A) HEK293-CAS9 cells expressing P4M-YFP, treated with or without U18. Bottom panels show enlarged views of PtdIns4P in a Golgi region.
C Quantitative analyses of P4M-YFP mean fluorescence intensity distributed in Golgi normalized to the cytoplasm under different conditions. Control: $n = 19$; U18: $n = 13$, sgPI4K2A: $n = 19$; sgPI4K2A+U18: $n = 17$; sgDHHC3: $n = 11$; sgDHHC3+U18: $n = 11$. * represents a significant difference ($P < 0.05$) between control and other non-U18 treated groups; # represents a significant difference ($P < 0.05$) between U18-treated and other U18-treated sgRNA groups.
D Confocal images of control (top) and $NPC1^{I1061T}$ (bottom) patient fibroblasts immunolabeled for DHHC3 and Giantin. Insets show enlarged views of DHHC3 and Giatin regions.
E Analysis of anti-DHHC3 mean fluorescence intensity in a Golgi region relative to cytoplasm. Control: $n = 19$; $NPC1^{I1061T}$: $n = 17$.
F Confocal images of control (1st column) and $NPC1^{I1061T}$ fibroblasts (2nd column) expressing mCherry-P4M or control fibroblasts expressing P4M-mCherry and GFP-DHHC3 (3rd column).
G Quantification of Golgi mCherry-P4M. Control: $n = 11$; $NPC1^{I1061T}$: $n = 14$; control+DHHC3: $n = 12$.
H Control or GFP-DHHC3 expressing tsA201 cells fixed and stained for PI4KIIα or PI4KIIIβ. Bottom panels show enlarged views of DHHC3, PI4KIIα, or PI4KIIIβ at Golgi regions.
I Quantification of PI4KIIα (left; control: $n = 42$, DHHC3: $n = 24$), or PI4KIIIβ (right; control: $n = 39$, DHHC3: $n = 26$) intensity relative to cytoplasm.
J Top: HEK293-CAS9 cells expressing P4M and either vehicle control, sgDHHC3, U18, and U18 with sgDHHC3. Bottom: expanded views of P4M in the black dashed rectangles.
K Control (left) and $NPC1^{I1061T}$ (right) patient fibroblasts expressing P4M-YFP (top row) or P4M-YFP and $DHHC3^{C157S}$ (DN-DHHC3; bottom row). Inset panels show enlarged views of P4M-YFP distribution at Golgi.
L Quantification of P4M-YFP signal in the Golgi region relative to cytoplasm. $NPC1^{I1061T}$: $n = 20$; $NPC1^{I1061T}$ + DN-DHHC3: $n = 14$.
M Confocal images of control (top row), $NPC1^{I1061T}$ (middle row), and $NPC1^{I1061T}$ treated with sgDHHC3 (bottom row) patient cells expressing P4M, LAMP1, and CAS9. Insets are zoomed regions from LAMP1-positive areas.
N Quantification of P4M changes at endomembranes. Control: $n = 149$, U18: $n = 251$, sgPI4KIIa +U18: $n = 131$, sgDHHC3+U18: $n = 271$. Each n represents a single enodolysosome.

Data information: All the data are expressed as mean ± SEM from individual cells with the exception of (N) which represents values from individual subcellular structures. Statistical analyses include two-way ANVOA (C, N), one-way ANVOA (G), unpaired t-test (E, I), or Mann–Whitney test (L). *$P < 0.05$; **$P < 0.01$; ****$P < 0.0001$. Source data are available online for this figure.

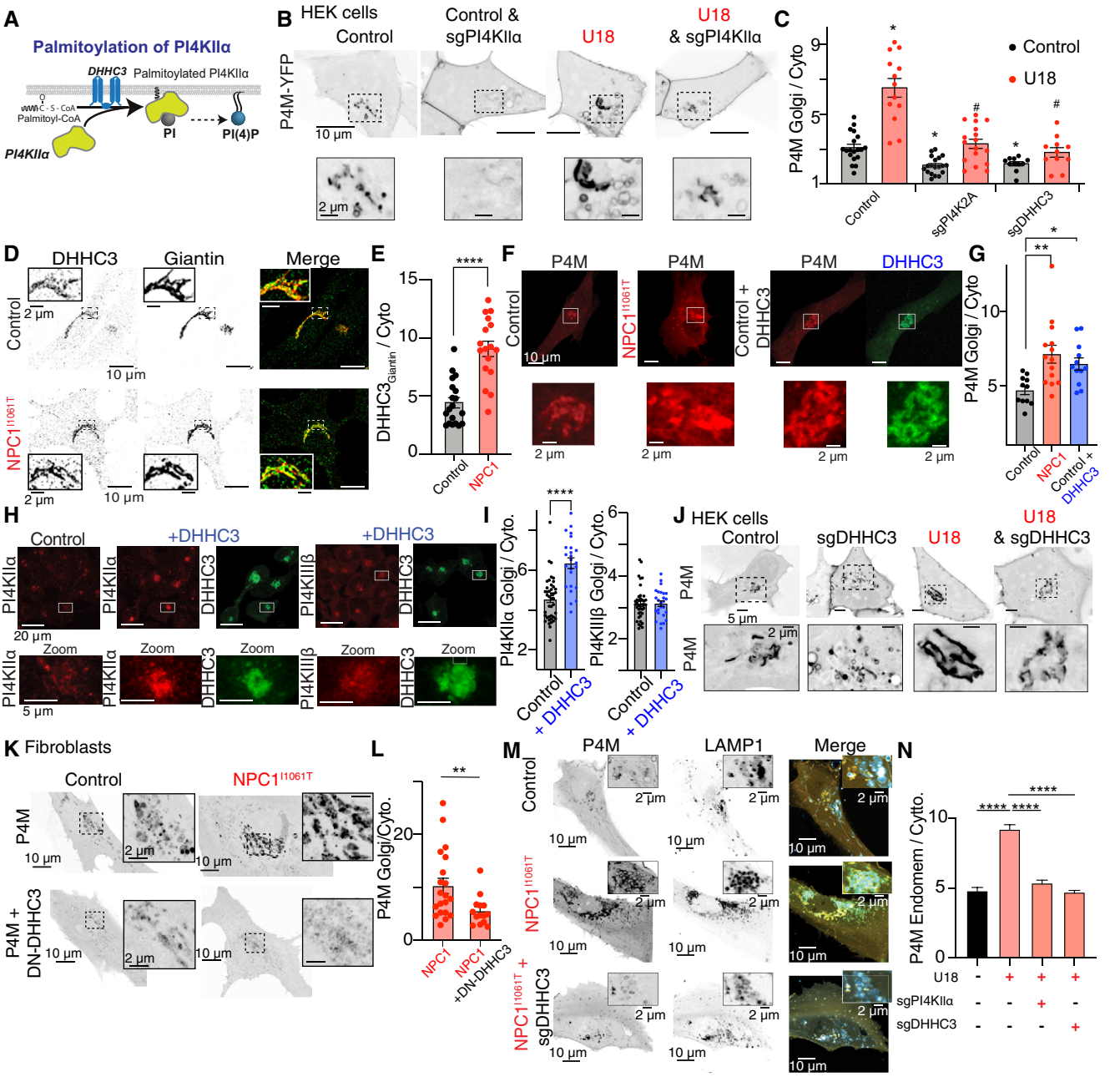

Figure 4.

ability to palmitoylate PI4KIIα in TGN membranes (Lu *et al*, 2012), and analyzed P4M and PI4KIIα distribution in control and NPC1^{I1061T} cells. Similar to DHHC3 knockdown, expression of DN-DHHC3 in NPC1^{I1061T} fibroblasts significantly reduced Golgi P4M (Fig 4K and L) and PI4KIIα (Fig EV3F) back to control levels. Thus, DHHC3-dependent recruitment of PI4KIIα appears to be part of the mechanism that increases Golgi PtdIns4P in NPC1 disease.

Ordinarily, PI4KIIα is fully palmitoylated and behaves almost entirely as an integral membrane protein (Barylko *et al*, 2009). Thus, the increase in PI4KIIα observed in NPC1 fibroblasts, or control cells overexpressing DHHC3, likely occurs due to a parallel reduction in PI4KIIα from a different membrane compartment(s). To begin testing this hypothesis, we fixed and stained control and NPC1^{I1061T} patient fibroblasts for endogenous PI4KIIα and markers of early endosomes (EEA1) and late endosomes (RAB7). Quantification of the subcellular localization between PI4KIIα and RAB7 revealed no clear differences between control and NPC1^{I1061T} cells, with a slightly reduced area of overall lap between signals (Fig EV4A–C). Contrary to this modest finding, analysis of PI4KIIα and EEA1 determined a 50% reduction in both the area of overlap and the intensity of signal from NPC1^{I1061T} cells relative to control (Fig EV4D–F). Therefore, at least one subcellular compartment loses a significant amount of PI4KIIα following loss of NPC1 function, that we suggest is recruited to Golgi via DHHC3. Future experiments are needed to fully dissect the molecular mechanism(s) underlying loss of PI4KIIα from early endosomes and subsequent increase at TGN membranes.

Finally, the increased localization of endogenous PI4KIIα to LAMP1-positive structures in NPC1 cells (Fig EV2E and F) prompted us to ask if DHHC3 localization was also increased at these membranes. To address this question, we fixed control and NPC1^{I1061T} patient cells and quantified the distribution of DHHC3 on LAMP1-positive membranes. Similar to Golgi membranes, the intensity of DHHC3 was significantly increased on lysosomes from NPC1^{I1061T} cells relative to control (Fig EV4G–I). To confirm a functional role for DHHC3 in regulating increases in lysosomal PtdIns4P in NPC1 disease, we treated HEK293-Cas9 cells with sgDHHC3 and compared the distribution of P4M relative to control cells. Consistent with DHHC3-dependent palmitoylation of PI4KIIα increasing PtdIns4P on lysosomal membranes in NPC1 disease, knockdown of lysosomal DHHC3 (Fig EV4J) in NPC1^{I1061T} cells or HEK293-Cas9 cells normalized lysosomal P4M signals back to control levels (Fig 4M and N).

Collectively, these data provide evidence that loss of NPC1 function initiates a signaling cascade that results in the recruitment of PI4KIIα to Golgi and lysosome membranes, via DHHC3-dependent palmitoylation, to increase PtdIns4P levels.

ACBD3-mediated recruitment of PI4KIIIβ to Golgi and lysosomes increases PtdIns4P levels in NPC1 disease

Having established a role for DHHC3-PI4KIIα increasing Golgi and lysosome PtdIns4P levels in NPC1 disease, we next investigated the mechanism underlying increased recruitment and/or activity of PI4KIIIβ to Golgi and endolysosomal membranes following NPC1 loss of function. To begin, we asked if PKD-mediated phosphorylation of PI4KIIIβ underlies the U18-dependent increase in Golgi PtdIns4P levels. PKD has a number of Golgi substrates, with its recruitment linked to the stimulation of PI4KIIIβ lipid kinase activity (Hausser *et al*, 2005) and OSBP localization (Nhek *et al*, 2010). Despite strong rationale for its potential involvement, inhibition of PKD activity failed to abrogate the U18-dependent increase in Golgi PtdIns4P levels (Appendix Fig S5A and B).

PI4KIIIβ is a soluble lipid kinase that can interact with a number of different proteins, including the multi-functional adaptor protein, Acyl-CoA-binding domain-containing 3 (ACBD3; Fig 5A) (Sasaki *et al*, 2012; Greninger *et al*, 2013; Chalupska *et al*, 2019). Therefore, we tested if ACBD3 is involved in increasing PI4KIIIβ levels at Golgi and endolysosome membranes. To begin, we quantified ACBD3 protein levels from control and NPC1^{I1061T} patient cells via Western blot and found cellular ACBD3 protein levels were significantly increased in NPC1 disease cells (Fig 5B). Subsequent immunofluorescence analyses of ACBD3 revealed a general pattern consistent with its reported localization at Golgi (Greninger *et al*, 2012; Sasaki *et al*, 2012) and lysosome membranes (White *et al*, 2016) (Fig 5C), with NPC1^{I1061T} patient cells having significantly elevated levels of ACBD3 at Golgi (Fig 5C and D) and endolysosomal regions compared to control (Appendix Fig S5C and D). To test whether increasing ACBD3 expression in control cells alters PtdIns4P and PI4KIIIβ to similar levels as NPC1 loss-of-function cells, we overexpressed GFP-ACBD3 and quantified Golgi P4M, PI4KIIα, and PI4KIIIβ. Consistent with a role for ACBD3 in mediating the increases in PtdIns4P observed in NPC1 loss-of-function cells, overexpressing GFP-ACBD3 in control cells increased P4M (Fig 5E and F) and PI4KIIIβ (Fig 5G and H), but not PI4KIIα, at Golgi membranes. Therefore, like DHHC3, increasing ACBD3 expression in control cells increases P4M and PI4KIIIβ to similar levels as NPC1 loss-of-function cells. To further probe the hypothesis that loss of NPC1 function drives ACBD3-dependent recruitment of PI4KIIIβ to elevate Golgi and endolysosome PtdIns4P levels, we knocked down ACBD3 ("sgACBD3") and quantified Golgi and lysosomal PtdIns4P levels. As before, treating HEK293-Cas9 cells expressing P4M-YFP with U18 increased Golgi and lysosome PtdIns4P levels (Fig 5I and J). Knocking down PI4KIIIβ ("sgPI4KIIIβ"; ~ 90% Fig EV3C) or ACBD3 ("sgACBD3"; ~ 65% Fig EV3A and Appendix Fig S5E and F) resulted not only in reduced steady-state PtdIns4P levels, but also significantly reduced U18-mediated elevations in Golgi and lysosomal PtdIns4P (Fig 5I and J; Appendix Fig S5G). Interestingly, Golgi PtdIns4P was refractory to U18-treatment when PI4KIIα and PI4KIIIβ were both knocked down (Fig 5J). We take this to mean that both PI4K enzymes not only regulate basal Golgi PtdIns4P levels, but also play important roles in mediating increases in Golgi PtdIns4P following loss of NPC function. While the underlying molecular elements of this signaling pathway may be more complex, we believe that collectively our data present a model where NPC1-dependent increases in ACBD3 protein levels at Golgi and lysosome membranes enhance recruitment of PI4KIIIβ to increase PtdIns4P synthesis.

Knocking down ACBD3 in NPC1^{I1061T} patient cells rescues cellular PtdIns4P phenotypes and prevents recruitment of mTORC1

A major cellular consequence of disease mutations in NPC1 is OSBP-mediated accumulation of cholesterol on the cytoplasmic leaflet of lysosome membrane which drives the recruitment of the master regulator of growth signaling, mTORC1, resulting in aberrant growth signaling (Lim *et al*, 2019). Under this model proposed by the Zoncu group, a key factor initiating OSBP-mediated cholesterol transfer and mTORC1 recruitment is the presence of lysosomal PtdIns4P which binds to OSBP's PH domain to tether ER-lysosome MCS. To date, there are no reports identifying the phosphoinositide metabolism elements required for cholesterol-dependent mTORC1 recruitment in NPC1 disease. With this in mind, we transfected patient cells with Cas9- and sgRNAs-directed against ACBD3, PI4KIIα, or PI4KIIIβ, while simultaneously monitoring cellular PtdIns4P levels with the P4M biosensor. In NPC1^{I1061T} patient cells, individual knockdown of either PI4KIIα or PI4KIIIβ significantly reduced both Golgi and lysosomal PtdIns4P levels (Fig 6A and B). It should be noted that sgPI4KIIIβ was more efficient at reducing Golgi PtdIns4P than sgPI4KIIα in NPC1^{I1061T} cells, suggesting a more prevalent role in maintaining Golgi PtdIns4P. This concept is further supported by immunofluorescence data that demonstrated a larger fold change in ACBD3 levels (Appendix Fig S5C and D), compared to DHHC3 (Fig EV4G–I), at lysosome membranes of NPC1^{I1061T} cells relative to control.

To test if ACBD3 is necessary for increased lysosomal PtdIns4P generation in NPC1 disease, we transfected sgACBD3 into NPC1^{I1061T} patient cells along with Cas9 and P4M-YFP. Similar, to HEK293-Cas9 cells treated with U18 (Fig 5I and J), transfecting sgACBD3 into NPC1^{I1061T} rescued PtdIns4P at Golgi regions levels back to control ranges and significantly reduced endolysosomal PtdIns4P levels (Fig 6A and B). To test if increases in lysosomal PtdIns4P production drives mTORC1 recruitment under NPC disease conditions, we transfected Cas9 and sgACBD3 into NPC1^{I1061T} patient cells and fixed and stained for endogenous mTORC1. Similar

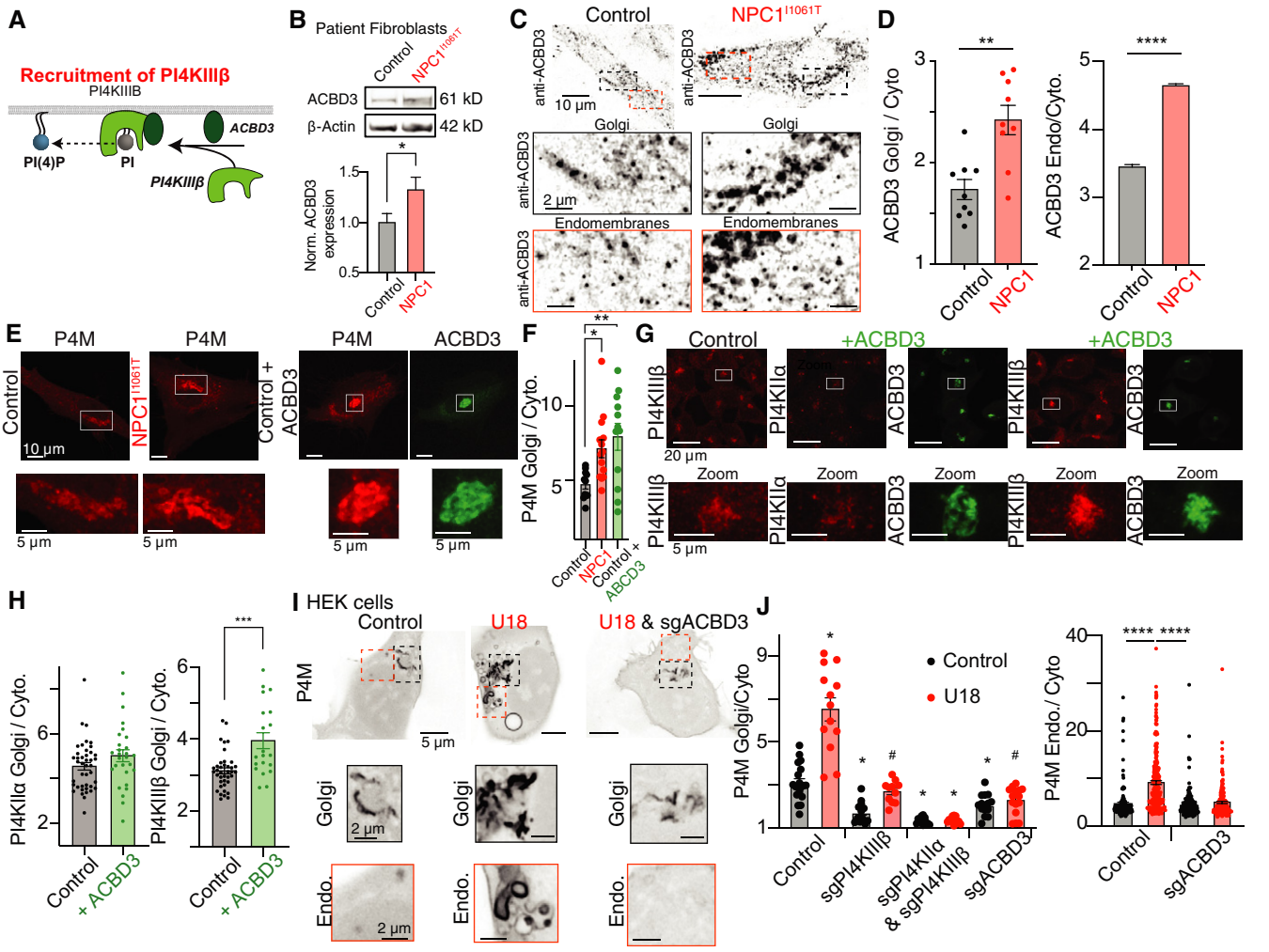

Figure 5. ACBD3-mediated PI4KIIIβ recruitment contributes to increased PtdIns4P levels at Golgi membranes following loss of NPC1 function.

A Diagram illustrating the Golgi recruitment mechanisms of PI4KIIIβ.

B Representative Western blot for ACBD3 in control and NPC1^{I1061T} patient fibroblasts. Protein levels were normalized to β-actin. Control: $n = 26$; NPC1^{I1061T}: $n = 27$. A paired t-test was used for the statistical analysis with $^{*}P < 0.05$.

C Confocal images of control and NPC1^{I1061T} patient fibroblasts immunolabeled for ACBD3. Black and orange squares show expanded views of anti-ACBD3 in Golgi and endomembrane compartments, respectively.

D Analyses of ACBD3 intensity distributed in Golgi (left graph; Control: $n = 9$; NPC1^{I1061T}: $n = 9$) or in endomembranes (right graph; Control: $n = 1{,}360$; NPC1^{I1061T}: $n = 1{,}645$ from 15 cells), normalized to the cytoplasm.

E Confocal images of control (1st column) and NPC1^{I1061T} fibroblasts (2nd column) expressing mCherry-P4M or control fibroblasts expressing P4M-mCherry and GFP-ACBD3 (3rd and 4th columns).

F Quantification of Golgi mCherry-P4M intensity relative to cytoplasm. Control: $n = 11$; NPC1^{I1061T}: $n = 14$; Control + ACBD3: $n = 12$.

G Confocal micrographs from control or GFP-ACBD3 expressing tsA201 cells fixed and stained for PI4KIIα or PI4KIIIβ. Bottom panels show enlarged views of ACBD3, PI4KIIα, or PI4KIIIβ at Golgi regions.

H Quantification of PI4KIIα (left; control: $n = 42$; ACBD3: $n = 28$), or PI4KIIIβ (right; control: $n = 39$; ACBD3: $n = 20$) intensity relative to cytoplasm.

I Confocal images of control and sgACBD3 HEK293-CAS9 cells expressing P4M-YFP, treated with or without U18. Bottom panels show enlarged views of PtdIns4P in Golgi and in endomembrane compartments.

J Quantitative analyses of P4M-YFP mean fluorescence intensity at Golgi (left graph) or endomembranes (right graph) normalized to the cytoplasm. * represents a significant difference ($P < 0.05$) between control and other non-U18 treated groups; # represents a significant difference ($P < 0.05$) between U18-treated and other U18-treated sgRNA groups. For left graph; Control: $n = 19$; U18: $n = 13$; sgPI4KIIIβ: $n = 12$; sgPI4KIIIβ + U18: $n = 11$; sgPI4KIIα + sgPI4KIIIβ: $n = 12$; sgPI4KIIα + sgPI4KIIIβ + U18: $n = 12$; sgACBD3: $n = 15$; sgACBD3+U18: $n = 16$. For right graph; control: $n = 149$; U18: $n = 251$; sgACBD3: $n = 138$; sgACBD3+U18: $n = 190$. Please note that "control" and "U18" datasets in Fig 5J are identical to those in Fig 4C. Data for all CRISPR experiments were collected on the same days.

Data information: All the data are expressed as mean ± SEM from individual cells with the exception of (D, right) and (J, right) which represents values from individual subcellular structures, $n = 10$ cells and $n = 13$ cells, respectively. Statistical analyses include unpaired t-test (D left graph, H left graph), Mann–Whitney test (D right graph, H right graph), or one-way ANOVA (F), $^{*}P < 0.05$; $^{**}P < 0.01$; $^{***}P < 0.001$; $^{****}P < 0.0001$. As determined by a Grubbs' test, with an alpha value of 0.05 (see methods), significant outliers were excluded from (J, right).
Source data are available online for this figure.

to previous reports (Lim *et al*, 2019), NPC1^{I1061T} disease mutations result in increased steady-state accumulation of mTORC1 at lysosome membranes (Fig 6C). Knocking down ACBD3 in NPC1^{I1061T} cells significantly reduced lysosomal mTORC1 recruitment back into a similar range as control cells (Fig 6C and D). Future experiments are required to carefully dissect the downstream consequences of decreased mTORC1 recruitment to lysosomal membranes following reductions in PtdIns4P levels. These data underscore the importance of lysosomal PtdIns4P metabolism for mTORC1 recruitment and present PI4KIIIβ and ACBD3 as key regulators of cellular growth signaling.

NPC1-dependent alterations in PI4K distribution are mediated via the SREBP pathway

The data presented thus far provide evidence linking loss of NPC1 function to the DHHC3- and ACBD3-mediated recruitment of PI4K enzymes to the TGN. The question remains, what is upstream of these recruiting factors that mechanistically links loss of NPC1 activity to recruitment of PI4K enzymes and increases in Golgi PtdIns4P? The major role of NPC1 is to facilitate the egress of cholesterol from luminal to cytoplasmic leaflets of the lysosomal membrane bilayer. Transported lysosomal cholesterol then serves as a signaling

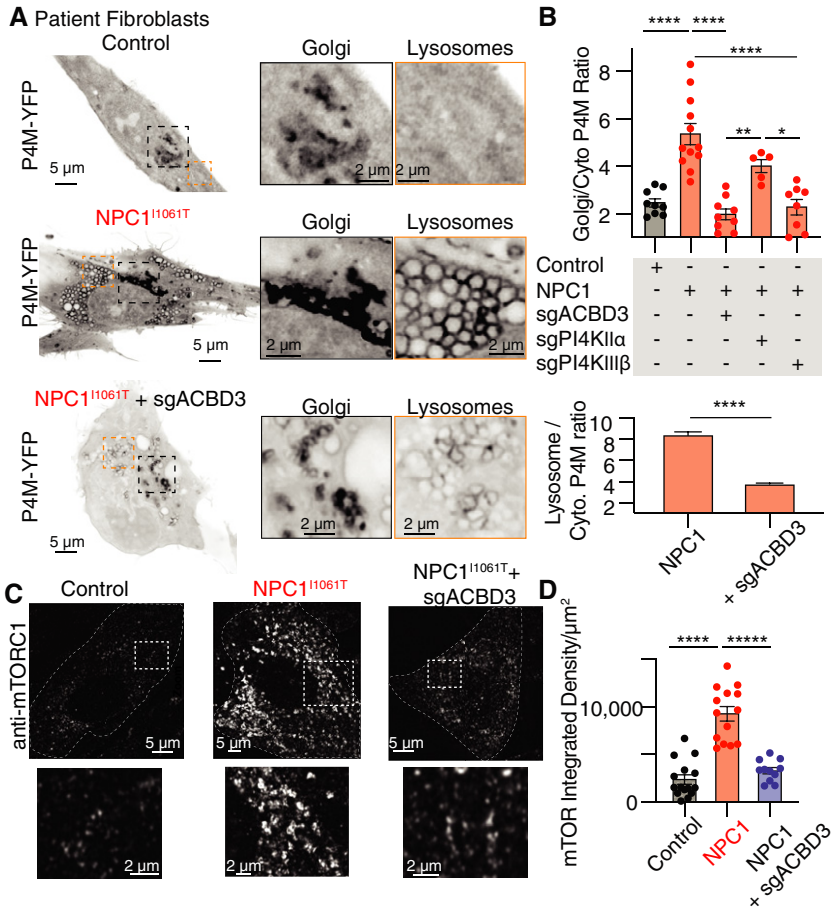

Figure 6. PtdIns4P produced by PI4KIIIβ regulates mTORC1 recruitment to endomembrane compartments.

A Confocal images of control, NPC1^{I1061T} and ACBD3-deleted NPC1^{I1061T} patient fibroblasts expressing P4M-YFP. Black and orange squares show expanded views of PtdIns4P in Golgi and endo/lysosomal compartments, respectively.

B Top graph: analysis of Golgi P4M-YFP intensity normalized to the cytoplasm in control and NPC1^{I1061T} patient fibroblasts and NPC1^{I1061T} fibroblasts lacking either ACBD3 ("sgACBD3"), PI4KIIα ("sgPI4KIIα") or PI4KIIIβ ("sgPI4KIIIβ"). Control: n = 9; NPC1^{I1061T}: n = 12; NPC1^{I1061T} + sgACBD3: n = 9; NPC1^{I1061T} + sgPI4KIIα: n = 5; NPC1^{I1061T} + sgPI4KIIIβ: n = 8. Bottom graph: analysis of P4M-YFP intensity in endomembrane compartments normalized to the cytoplasm in NPC1^{I1061T} patient fibroblasts. NPC1^{I1061T}: n = 406; NPC1^{I1061T} + sgACBD3: n = 172.

C Confocal images of control, NPC1^{I1061T} and ACBD3-deleted NPC1^{I1061T} patient fibroblasts immunolabeled with mTORC1 antibody. Bottom images show expanded views of mTORC1 immunolabeling in the regions indicated by the dashed squares in the main images. White dashed lines represent the outline of each cell.

D Quantification of mTORC1 mean integrated density normalized by cell area in control, NPC1^{I1061T} and ACBD3-deleted NPC1^{I1061T} patient fibroblasts. Control: n = 15; NPC1^{I1061T}: n = 14; NPC1^{I1061T}+sgACBD3: n = 11.

Data information: All the data are expressed as mean ± SEM from individual cells with the exception of (B, bottom) which represents values from individual subcellular structures. Statistical analyses include one-way ANVOA (B, top), Mann–Whitney test (B, bottom), and one-way ANOVA (D). *P < 0.05; **P < 0.01; ****P < 0.0001.
Source data are available online for this figure.

molecule (Castellano *et al*, 2017; Lim *et al*, 2019) that can be indirectly transported to the plasma membrane (Infante & Radhakrishnan, 2017) or directly transferred to the ER at ER-lysosome MCS (Rocha *et al*, 2009; Vihervaara *et al*, 2011). Levels of ER cholesterol are precisely monitored by a family of transcription factors called Sterol Regulator Element Binding proteins (SREBPs). Under conditions of reduced ER cholesterol levels, SREBPs are proteolytically cleaved and subsequently translocate to the nucleus where they upregulate the synthesis of many proteins (Brown & Goldstein, 1997; Rome *et al*, 2008). The general findings that *de novo* cholesterol synthesis, LDL uptake, and increased SREBP activity in $NPC1^{I1061T}$ patient cells have been established (Pentchev *et al*, 1985; Liscum & Faust, 1987; Frolov *et al*, 2003), therefore, we wanted to test the hypothesis that SREBP activation was upstream of PI4K recruitment to the Golgi.

To begin, we wanted to determine if SREBP impacts the transcription of DHHC3, ACBD3, PI4KIIα, and PI4KIIIβ. qPCR analysis of mRNA levels revealed that DHHC3 and ACBD3 levels were elevated in $NPC1^{I1061T}$ cells relative to control (Fig 7A), whereas PI4K levels were unchanged. Treating $NPC1^{I1061T}$ cells overnight with the specific SREBP site 1 protease inhibitor, PF-429242 (PF), normalized transcript levels back into control ranges. These data are in line with previously published microarray analysis detailing that ACBD3 is a target gene for SREBP (Rome *et al*, 2008) and suggest that SREBP may be responsible for the enhanced recruitment of PI4K enzymes to the Golgi following loss of NPC1 function. To test this idea, we overexpressed fluorescently tagged PI4Ks in tsA201 cells and monitored their distribution under conditions of altered NPC1 or SREBP function. Quantitative analysis of PI4KIIα distribution in cells treated concurrently with U18 and PF-429242 revealed identical levels of PI4KIIα at Golgi regions compared to vehicle-treated control cells (Fig 7B and C). Similar analysis performed on GFP-PI4KIIIβ expressing cells revealed that PI4KIIIβ recruitment to Golgi membrane was also refractory to U18 when treated concurrently with PF-429242 (Fig 7D and E). Parallel experiments investigating PtdIns4P metabolism revealed that U18-mediated increases in P4M intensity were also sensitive to SREBP pathway inhibition (Fig 7F and G).

To provide further evidence for SREBP's role in facilitating PI4K recruitment, we generated two additional datasets using overexpressed SREBP and cells lacking functional SREBP. Overexpressing SREBP increases the fractional amount of active, nuclear-localized SREBP and as such provides a way to activate SREBP, independently of NPC1. Similar to U18-treated or NPC1 disease mutations, cells overexpressing SREBP also had significantly elevated PI4KIIα and PI4KIIIβ at Golgi regions (Appendix Fig S6A–D). To further support a role for SREBP in mediating PI4K recruitment, we analyzed the distribution of P4M in control cells relative to $SCAP^{-/-}$ cells, that are unable to escort SREBP to the Golgi for processing to its "active" nuclear form (Rawson *et al*, 1999). Consistent with SREBPs involvement in mediating increases in Golgi and endomembrane PtdIns4P levels, P4M distribution in $SCAP^{-/-}$ cells was similar to control (Fig 7H and I and Appendix Fig S6E and F). It should also be noted that the distribution of SAC1 at the Golgi mirrored changes in Golgi PtdIns4P levels (Appendix Fig S7), likely ensuring the faithful maintenance of a steep PtdIns4P gradient for cholesterol transport. These independent datasets provide preliminary evidence that activation of SREBP maybe upstream of recruitment of PI4KIIα and PI4KIIIβ to Golgi and endolysosomal regions.

NPC1-mediated elevations in Golgi PtdIns4P increase Golgi to PM trafficking

We have identified a novel signaling axis that links NPC1-mediated cholesterol efflux to tuning of molecular contents of ER-TGN MCS. A key remaining question is with regard to the functional consequence of aberrant Golgi PtdIns4P in NPC disease. Golgi PtdIns4P plays a crucial role in the spatial and temporal recruitment of adaptor proteins to facilitate anterograde trafficking of cargo proteins destined for endosomes and the PM. While acute depletion of PtdIns4P prevents the exit of cargo from the Golgi destined for the PM, increased Golgi PtdIns4P leads to a malignant secretory phenotype in cancer (reviewed Waugh (2019)). To dissect a role for NPC1 in regulating secretory traffic, we first measured the distribution of cation-independent mannose 6-phosphate receptors (CI-MPR). These receptors are dynamically trafficked between the TGN and endosomes, as well as the PM and as such give a broad overview of secretory trafficking patterns (Dong *et al*, 2016). Control and $NPC1^{I1061T}$ patient cells were incubated with anti-CI-MPR (binds the extracellular region of CI-MPR at the PM) for 1 h, and the intracellular distribution of CI-M6PR antibody was detected by immunofluorescence. Quantitative analysis of the resulting confocal micrographs revealed that the CI-M6PR antibody was internalized with the receptor and accumulated at Giantin-positive Golgi membranes in control patient cells (Fig 8A, left middle row), as well as other non-giantin-positive internal membranes that likely correspond to endosomes (Fig 8A, left bottom row; Fig EV5A and B). In contrast, $NPC1^{I1061T}$ patient cells had a significantly higher accumulation of CI-MPR fluorescence at the Golgi (Fig 8A, right panel), coupled with decreased levels of fluorescence at peripheral vesicles (Fig 8A, right panel; Fig 8B for analysis). Thus, trafficking patterns are altered following loss of NPC1 function.

Figure 7. SREBP inhibition alleviates NPC1-dependent increase of PI4KIIα, PI4KIIIB, and PtdIns4P levels at Golgi membranes.

A qPCR analysis from control (black bars), $NPC1^{I1061T}$ (pink), and $NPC1^{I1061T}$ patient cells treated overnight with the SREBP inhibitor, PF-429242 (1 μM; blue bars). Error bars represent SEM from 6 technical and 2 biological replicates.

B Confocal images of tsA201 cells expressing PI4KIIα-GFP. Cells were treated with either vehicle (control), U18, or U18 and PF for 24 h prior imaging. Bottom panels show an enlarged view of the enzyme in a perinuclear area.

C Quantification of PI4KIIα-GFP mean fluorescence intensity in Golgi normalized to the cytoplasm. Control: $n = 12$; U18: $n = 14$; U18+PF: $n = 12$.

D, E Same as (B, C) but in tsA-201 cells transfected with PI4KIIIβ-GFP. Control: $n = 18$, U18: $n = 22$, U18+PF: $n = 23$.

F, G Same as (B, C) but in tsA-201 cells transfected with P4M-YFP. Control: $n = 39$, U18: $n = 42$, U18+PF: $n = 32$.

H, I Same as (F, G) but in wild-type and $SCAP^{-/-}$ CHO cells. Control: $n = 12$, U18: $n = 11$, $SCAP^{-/-}$ +U18: $n = 10$.

Data information: All the data are expressed as mean ± SEM from individual cells and all statistical analyses were conducted using a two-way ANOVA (A) or one-way ANVOA (C, E, G, I). *$P < 0.05$; **$P < 0.01$ and ****$P < 0.0001$.
Source data are available online for this figure.

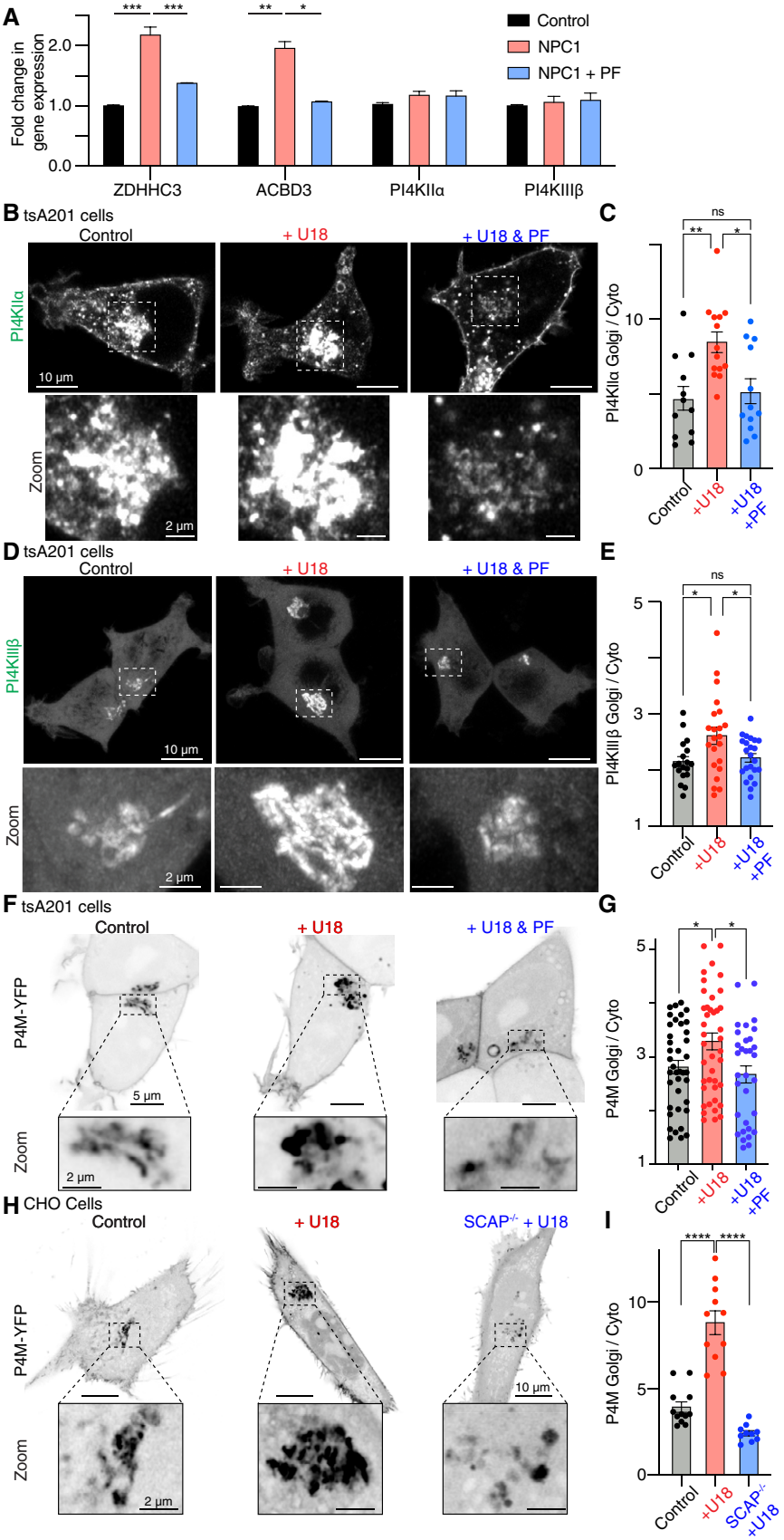

Figure 7.

To more specifically test if NPC1 loss of function can alter Golgi trafficking/sorting, we quantified the cellular distribution of the small GTPase ARF1. ARF1 has a well-established role in the assembly and budding of COPI vesicles at the Golgi, where its active form recruits coatomer for the formation of COPI-coated vesicles (Serafini *et al*, 1991; Palmer *et al*, 1993). With this in mind, analysis of expression patterns of ARF1-GFP revealed significantly greater accumulation at Golgi regions of NPC1^{I1061T} cells relative to control (Fig 8C and D). In addition, we also noticed more ARF1-positive tubular structures protruding from the Golgi region (Fig 8C, black arrows). These ARF1 tubules have previously been suggested to represent the major membrane flow out of the Golgi, with approximately one-third required to maintain plasma membrane growth (Bottanelli *et al*, 2017). These data, combined with increases in Golgi PtdIns4P (Fig 1), indicate that Golgi secretions may be accelerated following loss of NPC1 function.

To analyze and quantify transport characteristics in cells lacking functional NPC1, we utilized the retention using hooks (RUSH) assay (Boncompain *et al*, 2012). The RUSH system is based on the reversible interaction of a "hook" protein fused to streptavidin (Str) and stably anchored in a donor compartment with a reporter protein of interest fused to streptavidin-binding peptide (SBP). The addition of Biotin facilitates the release of the reporter from the organelle-localized hook and triggers the secretion of cargo. Fusion of a fluorescent protein to the reporter protein allows for the tracking and quantification of secretion rates between different organelles. Using the RUSH system, we retained cargo (tumor necrosis factor α (TNFα); TNF-SBP-mCherry), destined for the PM, in the ER (Str-KDEL) and analyzed the transport kinetics following the addition of Biotin (Fig 8E and F). Experiments performed at 37°C showed that TNFα-SBP-mCherry was initially retained in the ER (t = 0 s) through the interactions with Str-KDEL. Addition of Biotin facilitated the release of the reporter and its subsequent trafficking to Golgi apparatus within 15 min (Fig 8E and F; "control", black trace), before reaching the PM within ~ 25 min. Time series analysis of Golgi regions of interest from control cells revealed that the rate of TNFα-SBP-mCherry accumulation had a time constant of approximately 454 s (Fig 8G, bottom, Tau_{arrive} Golgi), an interval between 50% increase in intensity and 50% decrease in intensity (50:50 duration) of 1,200 s, and a rate of anterograde secretion to proximal membranes of approximately 1,548 s (Tau_{leave}). In contrast, cells treated overnight with U18, to inhibit NPC1 function, had significantly altered trafficking kinetics with the average time constant of Golgi accumulation (U18: Tau_{arrive} = 205 s), 50:50 duration (U18: 780 s), and secretion rate from the Golgi (U18: Tau_{leave} 294 s) all significantly faster (Fig 8E–G; red images, lines, and histograms). In addition, we analyzed TNFα-SBP-mCherry intensity from ER regions of interest and determined that the overall rate of secretion from the ER is similar between control and U18-treatment, with a key difference being that cargo is released sooner from U18-treated cells (Fig EV5C).

To understand how NPC1-dependent changes in trafficking may influence anterograde secretion toward the PM, we conducted similar experiments using TIRF microscopy (Fig 8H and I). In resting control cells, TNFα-SBP-mCherry was visualized within the TIRF footprint as discrete puncta, likely representing regions of close opposition between the ER and PM. Upon the addition of Biotin, there was an initial loss of intensity within the TIRF evanescent field which represents the cargo exiting the ER and trafficking to the Golgi (Fig 8H, black "control"). Within as little as 1,000 s, individual puncta, which we suggest are secretory vesicles fusing with the PM, reappeared within the TIRF field of view and were accompanied with a concurrent increase in intensity within a ROI encompassing the entire TIRF footprint. Analysis from control cells revealed the TIRF footprint intensity increased 2.5-fold with an average time constant 863 s (Fig 8H–J). Comparing control to U18-treated cells revealed that secretion of TNFα-SBP-mCherry from the ER to the PM was significantly faster (U18: Tau_{arrive} = 404 s), with more cargo trafficked to the PM per unit time (5.2-fold change; Fig 8I and J; red "+U18"). Similar U18-dependent increases in trafficking kinetics were observed with a VSVG plasmid that was released directly from the Golgi (Fig EV5D). Next, we tested a role for DHHC3 and ACBD3 in mediating U18-dependent increases in

Figure 8. SREBP inhibition alleviates vesicular trafficking defects in NPC1 disease.

A Confocal images of control and NPC1^{I1061T} patient fibroblasts immunolabeled for Giantin and CI-M6PR. Insets show expanded views of each immunolabeling in the Golgi region (upper insets) or centered on endomembranes (bottom inset, merged signals). Dashed gray and white lines represent the outline of each cell.

B Analysis of the mean area of M6P and Giantin colocalizing puncta (top graph; Control: n = 23; NPC1^{I1061T}: n = 18) and of their mean fluorescence intensity (bottom graph; Control: n = 18; NPC1^{I1061T}: n = 18) in control and NPC1^{I1061T} patient fibroblasts.

C Confocal images of control and NPC1^{I1061T} patient fibroblasts expressing ARF1-GFP. Insets show enlarged views of ARF1 in the Golgi area. Tubular structures were observed in NPC1^{I1061T} patient fibroblasts as indicated by the black arrows.

D Quantification of ARF1 fluorescence intensity in Golgi normalized to the cytoplasm in control and NPC1^{I1061T} patient fibroblasts. Control: n = 10; NPC1^{I1061T}: n = 11.

E Live confocal images of control and U18-treated cells transfected with Str-KDEL_TNF-SBP-mCherry. Images are taken at the indicated time points after biotin addition (at time 0 s) and the corresponding distribution of the TNF-SBP-mCherry within the cell is illustrated in the upper row.

F Average time course of mean TNF-SBP-mCherry fluorescence intensity in Golgi normalized to the initial fluorescence value. Shaded area represents the SEM. Control: n = 11; U18: n = 15.

G Analysis of the time constants for TNF-SBP-mCherry to reach and to leave the Golgi (Tau_{arrive} and Tau_{leave} Golgi, respectively) and the full duration at half maximum (50:50 Duration), calculated from the upper traces. Error bars represent SEM. Control: n = 10; U18: n = 13–15.

H Same as (E) except images are TIRF footprints of tsA201 cells treated either with vehicle (control) or with U18.

I Averaged time course of the mean plasma membrane fluorescence intensity normalized to the initial fluorescence value in tsA201 cells treated either with vehicle (control), with U18 alone, or together with PF. Shaded area represents the SEM, n = 9.

J Quantitative analysis of the time constants for TNF-SBP-mCherry to reach the plasma membrane (Tau_{arrive} PM) and the maximal change in fluorescence intensity relative to the initial fluorescence value (Intensity Change TIRF F/F_0). Error bars represent SEM. Control: n = 6–9; U18: n = 8–9; U18+PF: n = 5–9.

Data information: All the data are expressed as mean ± SEM from individual cells, and all statistical analyses were conducted using unpaired t-test with *P < 0.05, **P < 0.01, ***P < 0.001 and ****P < 0.0001.
Source data are available online for this figure.

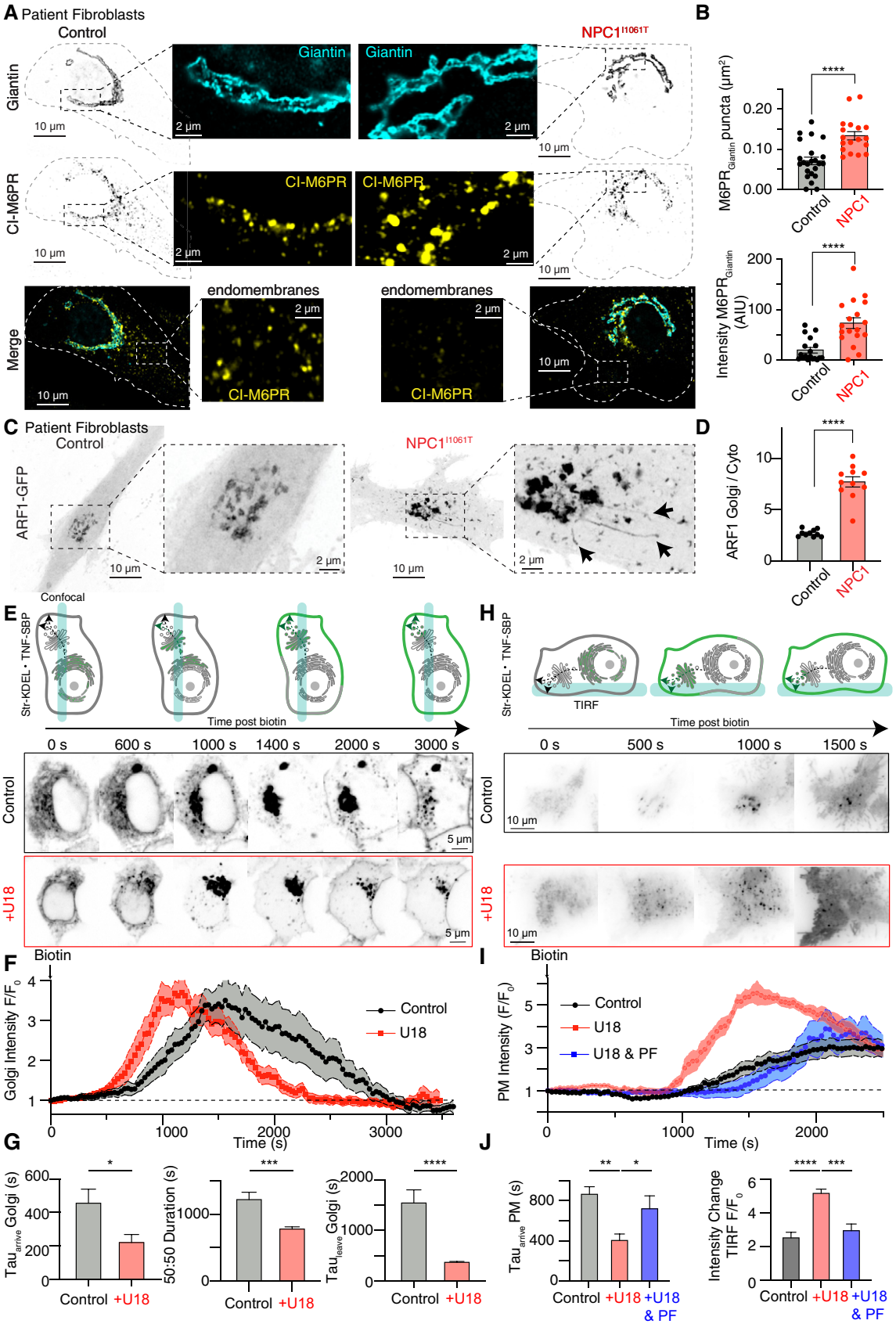

Figure 8.

Golgi secretion. To begin, we overexpressed DHHC3 and/or ACBD3 and found that while their individual expression increased trafficking rates to the PM, it was their dual expression that increased trafficking rates to the same extent as U18 (Fig EV5E). Conversely, knocking down either DHHC3 or ACBD3 abrogated U18-dependent increases in TNFα-SBP-mCherry secretion (Fig EV5F). Finally, we tested the involvement of the SREBP pathway in facilitating the increases in trafficking observed with U18 treatment. Consistent with its ability to regulate PI4K and PtdIns4P levels at the Golgi (Fig 7), SREBP overexpression accelerated secretion (Fig EV5G), while cells treated with a SREBP inhibitor were refractory to changes by U18 (Fig 8I and J; blue line) with the rate of traffic to the PM (PF: Tau_{arrive} = 720 s) and overall amount (2.9-fold change) of cargo delivered not statistically different from control. Collectively, these data support a role for NPC1 in tuning Golgi secretion through SREBP-dependent control of Golgi PtdIns4P.

Discussion

We have identified a novel signaling axis that connects NPC1 cholesterol efflux to the regulation of Golgi and lysosomal PtdIns4P levels (Appendix Fig S8). The molecular steps linking changes in the functional status of NPC1 to alterations in membrane PtdIns4P levels appear to involve cholesterol-dependent transcriptional changes in the recruitment machinery of PI4K metabolizing enzymes. Specifically, we have discovered that loss of NPC1 function increases DHHC3 and ACBD3 levels to enhance recruitment of PI4KIIα and PI4KIIIβ at Golgi and lysosomes, leading to elevations in membrane PtdIns4P. Crucially, we demonstrate this signaling node is conserved across multiple cell types, including patient cells and mouse neurons harboring the most prevalent NPC disease mutation. The importance of this signaling pathway in health and NPC disease is underscored by experiments demonstrating that loss of NPC1 function causes aberrant increases in anterograde trafficking and recruitment of the master growth regulator mTORC1 at the Golgi and lysosome membranes, respectively. Thus, NPC1 is a crucial rheostat capable of tuning cellular growth and rate of delivery of proteins to cellular membranes.

At the core of our findings is the recruitment of PI4KIIα and PI4KIIIβ to both Golgi and lysosome membranes following loss of NPC1 function. The presence of these PI4K enzymes at Golgi and lysosome membranes has been independently reported by multiple groups (Wong *et al*, 1997; Wei *et al*, 2002; Guo *et al*, 2003; Wang *et al*, 2003; Waugh *et al*, 2003). For PI4KIIα, significant evidence suggests a key role for palmitoylation-dependent recruitment to Golgi membranes by palmitoyl acyltransferases, such as DHHC3/7 (Lu *et al*, 2012). Our evidence for the involvement of DHHC3 in recruiting PI4KIIα to increase Golgi PtdIns4P is (i) DHHC3 enrichment at Golgi membranes, (ii) overexpression of DHHC3 increases PI4KIIα and PtdIns4P levels at Golgi membranes, (iii) knockdown of DHHC3 reduces Golgi PtdIns4P levels in NPC1 cells, and (iv) overexpression of a dominant-negative protein that lacks the ability to palmitoylate PI4KIIα, reduces PI4KIIα recruitment and elevations in PtdIns4P in NPC1 patient cells. Interestingly, we also find that knockdown of DHHC3 or PI4KIIα in NPC1-deficient cells significantly reduces lysosomal PtdIns4P, an observation consistent with its presence at lysosome membranes. This model is supported by our own report of DHHC3 and PI4KIIα on lysosomes, and independent reports of PI4KIIα (Lim *et al*, 2019), as well as other DHHC5 and DHHC20 palmitoyl acyltransferases (Liu *et al*, 2018; Lim *et al*, 2019), on lysosome membranes and suggests DHHC-dependent recruitment of PI4KIIα to lysosomes could be a mechanism for tuning lysosomal PtdIns4P levels. As noted, under normal cellular conditions PI4KIIα appears to be fully palmitoylated and essentially acts as an integral membrane protein. This means that NPC1-mediated increases in Golgi or lysosome PI4KIIα likely occur as a consequence of reductions in PI4KIIα at other subcellular compartments. Our data suggest loss of PI4KIIα from early endosome compartments may provide the substrate for DHHC3 to elevate levels at Golgi and lysosome membranes. Future experiments are required to rigorously test this hypothesis.

In the case of PI4KIIIβ, our analysis details an important role for ACBD3 in facilitating the increases in Golgi and lysosome PtdIns4P, consistent with reports specifying interactions between the N-terminus of PI4KIIIβ and ACBD3 (Sasaki *et al*, 2012; Klima *et al*, 2016). Despite its crucial role in recruiting PI4KIIIβ to the Golgi, there are only a few reports of it being localized to lysosome membranes (White *et al*, 2016; Liu *et al*, 2018). Our super-resolution imaging analysis determined that the cellular fraction of ACBD3 coincident with LAMP1 and PI4KIIIβ levels are both significantly elevated at lysosome membranes following loss of NPC1 function. Furthermore, we find that knockout of either ACBD3 or PI4KIIIβ significantly reduces PtdIns4P levels across different cells lacking NPC1 function. These data are consistent with a NPC1-dependent mechanism that facilitates ACBD3-mediated recruitment of PI4KIIIβ to lysosome membranes. It should be noted that we also see an elevation in the abundance of ARF1 at Golgi membranes. This is important because it has been proposed that ACBD3 controls the Golgi recruitment of PI4KIIIβ, which in turn recruits c10orf76 to influence the dynamics and localization of Arf1-GTP, to activate PI4KIIIβ (McPhail *et al*, 2019). Thus, the observed increases in Golgi PI4KIIIβ and PtdIns4P could be under the dual regulation of ACBD3 and ARF1 in NPC1 disease. It should be noted that in our experiments we use overexpression and knockdown of proteins to test a role for ACBD3 and DHHC3 in recruiting PI4K enzymes to Golgi and lysosomal membranes. These approaches offer ways to dramatically increase or decrease protein levels to test their involvement in facilitating increases in PtdInsP levels following loss of NPC1 function. Future experiments, that precisely titrate protein levels to the same magnitude as observed in NPC1 loss of function cells, will be required to fully test whether changes in recruitment of these proteins to Golgi or lysosome membranes are necessary or sufficient for the observed changes in PtdInsP levels, trafficking, and mTORC recruitment.

A key question remaining is the molecular timing of PtdIns4P increases at Golgi and lysosome membranes following loss of NPC1 function. We offer three simple, and certainly not exhaustive models. First, the simplest interpretation is that both enzymes are concurrently recruited to each organelle membrane to elevate PtdIns4P levels. This model is supported by the presence of recruitment machinery and enzymes at both organelles. An alternative model involves PI4KIIα/IIIβ synthesizing PtdIns4P only at Golgi membranes, with exiting vesicles entering the endolysosomal pathway having excess PtdIns4P. If correct, the fraction of PI4KIIα/IIIβ we observe on lysosomes would merely be coincident with PtdIns4P elevations and thus would likely not have local access to their PtdIns substrate. In a final, sequential model, influenced by the Balla group (Jović *et al*, 2012), ACBD3-PI4KIIIβ generates PtdIns4P at the Golgi, to allow for efficient exit of cargo destined for lysosomes, while DHHC3-PI4KIIα generates PtdIns4P on late endosomes

to enable efficient cargo transport to lysosomes. Here, the compound elevations in PtdIns4P levels would sequentially increase PtdIns4P levels across the endolysosomal pathway. Each of these models offers several interesting avenues for future exploration.

An intriguing observation in the course of our studies is the fluidity of proteins within membrane-membrane contact sites (MCS). While much research has characterized the identity of many of the proteins within ER-TGN and ER-lysosome MCS, little is known about the molecular choreography of these proteins and how exactly they are modified during pathophysiological conditions. Here we show that loss of NPC1 function leads to a functional reorganization of key components of the cholesterol/PtdIns4P cycle and represents one of the first reported examples of fine-tuning of these transfer portals in disease. Our data reveal enhanced recruitment of OSBP, VAPA, and SAC1 to ER-TGN MCS in cells harboring NPC1 disease mutations. We suggest the molecular rearrangement of these MCS proteins likely occurs downstream of PI4K-dependent generation of Golgi PtdIns4P. In our model, increased Golgi or lysosome PtdIns4P levels would recruit OSBP through binding of its PH domain to PtdIns4P, while interactions with VAP would engage the ER. Increased tethering of OSBP at MCS would amplify PtdIns4P and cholesterol transport to ER and donor membranes, respectively. This leaves SAC1 the crucial task of dephosphorylating transferred PtdIns4P to PtdIns on ER membranes. This key step ensures the maintenance of the steep PtdIns4P gradient and positions SAC1 is as key regulator of the OSBP cycle. Key questions remain for the cholesterol/PtdIns4P cycle in NPC1 disease, such as, (i) what effect does altered NPC1 and OSBP function have on TGN cholesterol? (ii) What influence do cholesterol levels at ER and TGN membranes have on cholesterol sensitive proteins like PI4KIIα (Waugh *et al*, 2006) or membrane proteins like VAPA and SAC1, that are well positioned to sense variations in cholesterol levels (Wakana *et al*, 2021), and (iii) how are PI4KIIα and IIIβ spatially and temporally coupled at ER-TGN MCS to organize cholesterol and PtdIns4P transport?

In the context of NPC1 disease, as in other cancers/aging/neurological disorders (Condon & Sabatini, 2019), the recruitment of mTORC1 to lysosome membranes would initiate aberrant growth pathways leading to inhibition of essential autophagic clearing functions and buildup of toxic metabolites. In NPC disease, the sequence of events leading to mTORC1 recruitment to lysosome membranes begins with reduced cholesterol efflux across the lysosome membrane leading to the initiation of the following pervasive signaling reaction: (i) increased PI4K-dependent production of PtdIns4P (this manuscript), (ii) increased lysosomal PtdIns4P facilitates increased engagement of OSBP at ER-lysosome MCS (Lim *et al*, 2019), leading to (iii) a steeper PtdIns4P gradient to drive cholesterol transport from the ER to lysosome membrane (Mesmin *et al*, 2013; Lim *et al*, 2019), thereby (iv) assisting in the recruitment of mTORC (Castellano *et al*, 2017; Lim *et al*, 2019). It should be noted that previous work, using similar cell lines, demonstrated that both recruitment and downstream activity of mTORC1 are increased following loss of NPC1 function (Castellano *et al*, 2017; Lim *et al*, 2019). We show that mTORC1 recruitment is altered following knockdown of ACBD3, careful investigations are still required to dissect the downstream consequences of PI4K-mediated mTOR activity. mTOR has also been demonstrated to contribute to SREBP activation, by controlling the nuclear entry of Lipin-1 (Peterson *et al*, 2011). Activated mTORC1 has been shown to phosphorylate lipin 1 to retain it in the cytoplasm, allowing nuclear SREBP binding to target genes resulting in increased lipogenesis. In the context of our data detailing a potential role for SREBP in enhancing the recruitment of PI4K enzymes, mTORC1 activation may remove an inhibitory brake on SREBP target genes, to increase lysosomal PtdIns4P thereby strengthening and perpetuating mTORC1 recruitment.

It remains to be fully determined if NPC1-dependent increases in Golgi membrane PtdIns4P levels represent a cellular signaling pathway that compensates for altered cholesterol homeostasis to preserve cerebellar neuron integrity or destructively contributes to the death of vulnerable Purkinje neurons (Praggastis *et al*, 2015). Given that PI4K enzymes and PtdIns4P have been implicated across a wide range of neuronal functions and pathologies, including Gaucher disease (Jović *et al*, 2012), spinocerebellar degeneration (Simons *et al*, 2009), myelination (Alvarez-Prats *et al*, 2018), and Schizophrenia (Jungerius *et al*, 2008; Houlihan *et al*, 2009), our results suggest that the NPC1-dependent elevations in Golgi PtdIns4P leading to enhanced anterograde Golgi trafficking will likely be deleterious to neuronal fidelity. Lessons from cell biology and cancer inform us of the importance of regulated PtdIns4P-dependent trafficking events at the Golgi (reviewed Waugh (2019)) and how their dysfunction leads to alterations in the PtdIns4P protein interactome, a malignant secretory phenotype, and tumor progression.

In conclusion, we propose that lysosomal NPC1-mediated cholesterol efflux modulates the SREBP-dependent recruitment of PI4K enzymes to control the molecular organization of ER-TGN and ER-lysosome membrane contact sites, thereby tuning mTORC-dependent growth conditions and anterograde trafficking in health and disease. Collectively, this information presents intriguing possibility that similar to cancer, targeting these enzymes, their chaperones, substrates, and/or products in neurodegenerative disease, may offer therapeutic checkpoints for devising strategies to slow neuronal death and hence disease progression.

Materials and Methods

Reagents and Tools table

Reagent or resource	Source	Identifier
Antibodies		
Rabbit polyclonal PI4KIIα	Abcam	Cat# ab71824; RRID: AB_1269758
Rabbit polyclonal PI4KIIα	P. De Camilli, Yale University School of Medicine, New Haven, CT	N/A
Mouse monoclonal PI4KIIα	Santa Cruz	Cat# sc-390026

Reagents and Tools table (continued)

Reagent or resource	Source	Identifier
Rabbit polyclonal PI4KIIIβ	Abcam	Cat# ab109418; RRID: AB_10861028
Mouse monoclonal PI4KIIIβ	BD Biosciences	Cat# 611816; RRID: AB _399296
Sheep polyclonal TGN46	Bio-Rad	Cat# AHP500GT; RRID: AB_2203291
Mouse monoclonal TGN46	Novus	Cat# NBP1-49643; RRID: AB_10011762
Mouse monoclonal EEA1	BD Biosciences	Cat# 610456, RRID: AB_ 397829
Mouse monoclonal RAB7	Santa Cruz Biotechnology	Cat# sc-271608; RRID: AB_10649046
Mouse monoclonal β-actin	Thermo Fisher Scientific	Cat# MA1-91399, RRID: AB_2273656
Mouse monoclonal VAPA	J. Trimmer, UC Davis, Davis, CA	N/A
GAPDH	Proteintech	10494-1-AP
Rabbit polyclonal OSBP	Atlas antibodies	Cat# HPA039227; RRID: AB_2676401
Rabbit polyclonal DHHC3	Abcam	Cat# ab31837; RRID: AB_742236
Rabbit polyclonal SAC1	Atlas Antibodies	Cat# HPA069869; RRID: AB_2686216
Mouse monoclonal ACBD3	Santa Cruz Biotechnology	Cat# sc-101277; RRID: AB_2273355
Mouse monoclonal Giantin	Abcam	Cat# ab37266; RRID: AB_880195
Rabbit polyclonal Giantin	BioLegend	Cat# 924302; RRID: AB_2565451
Mouse monoclonal Lamp1	Abcam	Cat# ab25630; RRID: AB_470708
Rabbit polyclonal Lamp2	Invitrogen	Cat# PA1-655; RRID: AB_2134625
Rabbit monoclonal mTOR	Cell Signaling Technology	Cat# 2983S
Goat anti-Mouse, Alexa Fluor 647	Invitrogen	Cat# A-21236; RRID: AB_141725
Goat anti-Rabbit, Alexa Fluor 488	Invitrogen	Cat# A-11034; RRID: AB_2576217
Donkey anti-Sheep, Alexa Fluor 555	Invitrogen	Cat# A-21436; RRID: AB_2535857
Goat anti-Rabbit 680RD	LI-COR Biosciences	Cat# 926-68071; RRID: AB_10956166
Goat anti-Mouse 800CW	LI-COR Biosciences	Cat# 925-32210, RRID: AB_2687825
Chemicals, peptides, and recombinant proteins		
B27	Gibco	Cat#17504-044
Glutamax	Gibco	Cat#35050-061
Cytosine-D-arabinofuranoside	Millipore	Cat#251010
U18666A	Sigma-Aldrich	Cat#U3633
PF-429242	Tocris	Cat#3354
Lipofectamine 2000	Invitrogen	Cat#11668-027
Lipofectamine LTX	Invitrogen	Cat#15338-030
Lipofectamine RNAiMAX	Invitrogen	Cat#13778-030
Paraformaldehyde	Electron Microscopy Sciences	Cat#15710
Glutaraldehyde	Sigma	Cat# G7651
Filipin	Sigma	Cat#F9765
SEA BLOCK Blocking Buffer	Thermo Scientific	Cat# 37527
Complete Mini protease inhibitor cocktail	Roche	Cat# 11836170001
PowerUp SYBR Green Master Mix	Thermo Fisher Scientific	Cat#A25742
Critical commercial assays		
Pierce BCA Protein Assay Kit	Thermo Fisher	Cat# 23225
AffinityScript QPCR Synthesis Kit	Agilent technologies	Cat#600559
RNeasy Plus Mini Kit	Qiagen	Cat#74134
Experimental models: cell lines		
Control patient-derived fibroblasts	Coriell Institute	Cat# GM05659
NPC1^{I1061T} patient-derived fibroblasts	Coriell Institute	Cat# GM18453

Reagents and Tools table (continued)

Reagent or resource	Source	Identifier
NPC1$^{-/-}$ CHO cell line	Millard *et al* (2000)	N/A
HEK293 Cas9 cell line	ATCC	Cat# CRL-1573Cas9
HEK293 eGFP-Sac1	Zewe *et al* (2018)	N/A
tsA201 Cell Line	Sigma	Cat# 96121229
Experimental models: organisms/strains		
E18 mouse embryos	JAX	
Oligonucleotides		
sgRNA targeting PI4K2A sequence: CCATTGACCGAGTGAAGTCC	Integrated DNA Technologies	N/A
sgRNA targeting PI4K3B sequence: CCACTCAACGACACTCCCGT	Integrated DNA Technologies	N/A
sgRNA targeting ACBD3 sequence: GAGCTTGACAAACTCCACCA	Integrated DNA Technologies	N/A
sgRNA targeting DHHC3 sequence: CGGAATTGTGTTCAACCTGC	Integrated DNA Technologies	N/A
PrimeTime qPCR PI4KIIα Primers:	Integrated DNA Technologies	Hs.PT.58.733616
PrimeTime qPCR PI4KIIIβ Primers:	Integrated DNA Technologies	Hs.PT.58.14990511
PrimeTime qPCR ACBD3 Primers	Integrated DNA Technologies	Hs.PT.58.26724987
PrimeTime qPCR DHHC3 Primers	Integrated DNA Technologies	Hs.PT.58.45384099
PrimeTime qPCR HPRT Primers	Integrated DNA Technologies	Hs.PT.58v.45621572
Recombinant DNA		
P4M-YFP	Kruse *et al* (2016)	N/A
pGFP-P4M	Hammond *et al* (2014)	
mCherry-P4M	Hammond *et al* (2014)	N/A
GFP-tagged PI4KIIα and PI4KIIIβ	Balla *et al* (2002)	N/A
GFP-DHHC3	This paper	N/A
GFP-ACBD3	This paper	N/A
HA-tagged DHHC3, DHHC3 (C157S), DHHC7, DHHC7 (C160S) and GSD	Fukata *et al* (2004)	N/A
LAMP1-RFP	Addgene	Cat#1817
LAMP1-mGFP	Addgene	Cat#34831
LAMP1-CFP	Komatsu *et al* (2006)	N/A
SEC61β-mCherry	Dickson *et al* (2016)	N/A
OSH1-GFP	Szentpetery *et al* (2010)	N/A
2xFLAG-SREBP-1a	Addgene	Cat#26801
Str-Golgin84_VSVG-SBP-EGFP	Addgene	Cat#65305
pTGN38-CFP	Szentpetery *et al* (2010)	
Str-KDEL_TNF-SBP-mCherry	Addgene	Cat#65279
Software and algorithms		
ImageJ	NIH	https://imagej.nih.gov/ij/
Micro-manager	NIH	https://micro-manager.org
ZEN imaging software	Zeiss	RRID: SCR_013672
MassLynx software	Waters	RRID: SCR_014271
GraphPad Prism8	GraphPad	RRID:SCR_002798
Other		
Polyacrylamide Bis-Tris gel	Invitrogen	Cat# NW04120BOX
Polyvinylidene difluoride membrane	Life Technologies	Cat# LC2000

Methods and Protocols

Cell culture

All the cell lines were incubated at 37°C and 5% CO_2 and subcultured twice weekly. Patient fibroblasts from an apparently healthy male (control) and a male with a homozygous mutation in $NPC1^{I1061T}$ were purchased from Coriell Institute and were grown in Eagle's Minimum Essential Medium (MEM) supplemented with 2 mM L-glutamine, 10% FBS and 0.2% penicillin/streptomycin. Control, $NPC1^{-/-}$ (Millard *et al*, 2000), and SRD-13A CHO cells (Rawson *et al*, 1999) ($SCAP^{-/-}$) (kindly provided by D. Ory, Washington University, St. Louis, MO), HEK293 cells that stably express Cas9 (HEK293-CAS9) were purchased from ATCC (CRL-1573Cas9). tsA201 cells were cultured in DMEM-based proliferation medium containing 10% FBS and 0.2% penicillin/streptomycin. HEK293 cells stably expressing eGFP11-Sac1 and eGFP11-Sec61β were kindly provided by G. Hammond (Zewe *et al*, 2018) (University of Pittsburgh School of Medicine, Pittsburgh, PA) and were cultured in the same way as tsA201 cells. COS7 cells were a kind gift from Dr. Jodi Nunnari (University of California, Davis). All cells were seeded on #1.5 glass coverslips 2 to 4 days prior imaging or fixation. Hippocampal neurons were isolated and cultured as previously described(Tiscione *et al*, 2019). Briefly, hippocampi were dissected from E18 mouse embryos and treated for 20 min at 37°C in Hank's solution containing 0.25% trypsin, followed by mechanical dissociation. Isolated neurons were plated on coverslips coated with poly-L-lysine and cultured in Neurobasal supplemented with B27, Glutamax, 5% FBS, and 0.2% penicillin/streptomycin. After 7 days *in vitro* (DIV), cytosine-D-arabinofuranoside (251010; Millipore) was added to neuronal cultures to inhibit astrocyte growth. For inhibition of NPC1 activity and SREBP pathway, cells were treated for 24 h prior imaging with 10 μM U18666A and/or 10 μM PF-429242, respectively.

Plasmid and sgRNA transfections

Plasmids encoding the following proteins were used: P4M-YFP (Kruse *et al*, 2016), mCherry-P4M (Hammond *et al*, 2014), eGFP-P4M (Hammond *et al*, 2014), GFP-tagged PI4KIIα and PI4KIIIβ (kind gift from Tamas Balla, NIH, Bethesda, MD) (Balla *et al*, 2002), HA-tagged DHHC3, DHHC3 (C157S), DHHC7, DHHC7 (C160S) and GSD (kindly provided by M. Fukata, National Institute for Physiological Sciences, Okazaki, Japan) (Fukata *et al*, 2004), pLAMP1-mCherry, pLAMP1-mGFP, OSH1-GFP (Szentpetery *et al*, 2010), 2xFLAG-SREBP-1a (Addgene: 26801), Str-Golgin84_VSVG-SBP-EGFP, Str-KDEL_TNF-SBP-mCherry (Boncompain *et al*, 2012). In addition, GFP-DHHC3 (Accession No: NM_016598.3) and GFP-ACBD3 (NM_022735.4) were cloned into pcDNA3.1(+)-N-eGFP: 5′: cloning site KpnI, 3′ Cloning Site: BamHI. Transfections of cDNAs (0.5 to 1 μg) were performed 24 h prior imaging using either Lipofectamine 2000 for hippocampal neurons, CHO and tsA201 cells, or Lipofectamine LTX for fibroblasts. To generate gene knockouts, short guide RNAs targeting *PI4KIIα*, *PI4KIIIβ*, *DHHC3*, and *ACBD3* were transfected in Cas9-expressing HEK293 cells along with a fluorescent transfection marker using Lipofectamine RNAiMAX and incubated for 48–72 h before imaging. Reduction in gene products was validated by Western blot and immunofluorescence analysis (Fig EV3). A limitation of this approach is that it does not generate knockout cell lines rather results in 70–90% knockdown of protein products.

Filipin staining and imaging

Cholesterol was stained according to a previously described procedure (Vivas *et al*, 2019). Cells were first fixed with 4% paraformaldehyde and 0.1% glutaraldehyde in phosphate-buffered saline (PBS) for 10 min at room temperature, before being incubated for 2 h at room temperature in PBS containing filipin at 3 mg/ml. After 5 × 5 min washes in PBS, cells were imaged in PBS under a Zeiss 880 AiryScan confocal microscope. Filipin fluorescence was visualized using 405 nm excitation.

Immunofluorescence labeling

Cells were fixed for 10 min at room temperature in PBS with 3% paraformaldehyde and 0.1% glutaraldehyde and blocked for 1 h in 50% SEA BLOCK Blocking Buffer and 0.5% Triton X-100 in PBS. After 5 × 5 min washes in PBS washes, cells were incubated overnight at 4°C in 20% SEA BLOCK and 0.5% Triton X-100 in PBS with the following primary antibodies: rabbit polyclonal *PI4KIIα* (1:250, kindly provided by Pietro De Camilli, Yale University School of Medicine, New Haven, CT), mouse monoclonal PI4KIIα (1:50), mouse monoclonal PI4KIIIβ (1:25), sheep polyclonal TGN46 (1:100), mouse monoclonal TGN46 (1:400), mouse monoclonal EEA1 (1:25), mouse monoclonal RAB7 (1:50), rabbit polyclonal OSBP (1:100), mouse monoclonal VAPA (hybridoma culture supernatant: 1:5; kindly provided by J. Trimmer, UC Davis, Davis, CA), rabbit polyclonal DHHC3 (1:50), rabbit polyclonal SAC1 (1:100), mouse monoclonal ACBD3 (1:50), mouse monoclonal Giantin (1:500), rabbit polyclonal Giantin (1:100), rabbit polyclonal Lamp2 (1:00), and mouse monoclonal Lamp1 (1:20). For immunofluorescence detection, cells were incubated with Alexa Fluor 488 anti-rabbit (1:1,000), Alexa Fluor 555 anti-Sheep (1:1,000), and Alexa Fluor 647 anti-mouse (1:1,000) secondary antibodies for 1 h at room temperature in the dark.

Super-resolution confocal microscopy

Imaging was conducted at room temperature with a Zeiss LSM880 confocal laser scanning microscope equipped with a Plan-Apochromat 63× Oil DIC M27 objective (N.A. 1.4) and a super-resolution Airyscan detection unit. Images of GFP/Alexa-488, YFP, mCherry, and Alexa-647 were collected using the 488, 514, 594, and 633 nm excitation lines, respectively, with multicolor images sequentially acquired. Live and fixed cells were imaged in PBS or Ringer's solution (in mM, 160 NaCl, 2.5 KCl, 2 $CaCl_2$, 1 $MgCl_2$, 10 HEPES, and 8 D-Glucose). For all acquisitions, images were taken at 0.5 μm depth intervals within the cell and were subsequently corrected using the Airyscan processing toolbox in ZEN software. Analysis was carried out with ImageJ (NIH, Bethesda, MD, USA). Briefly, z-stack images were collapsed to single maximum intensity projection images. After background subtraction, mean fluorescence intensity was measured within a region of interest (ROI) and normalized to the cytoplasm mean fluorescence intensity. For colocalization / overlap analyses, binary masks of TGN38/46, Giantin, or Lamp1 images were used to measure P4M, PI4K enzymes, VAPA, OSBP, SAC1, and SEC61β fluorescence intensities.

RUSH trafficking assay

Membrane trafficking was assessed by means of the retention using selective hooks (RUSH) system (Boncompain *et al*, 2012). Briefly, live imaging in tsA201 cells expressing Str-KDEL_TNF-SBP-mCherry

or Str-Golgin84_VSVG-SBP-EGFP was performed using a combined Andor W-1 spinning disk confocal microscope and Olympus Cell total internal reflected fluorescence (TIRF) system, equipped with a Photometrics Prime 95B camera and a stage-top temperature and CO_2-controlled incubator (Okolab). Cells were excited either with 488-nm or 561-nm lasers, and confocal or TIRF images were collected through a 63× (1.4 NA) Olympus objective, using Micromanager software. All images were acquired at 37°C in phenol red-free DMEM with a frequency of 2 frames per min. D-Biotin (80 μM) was added in the experimental chamber after 1–2 min of acquisition. Image analysis was performed using ImageJ software.

Quantitative polymerase chain reaction

The RNA transcripts from control and NPC1 patient fibroblasts were first extracted using RNeasy Plus Mini Kit before being converted into cDNA with an AffinityScript qPCR cDNA Synthesis Kit. Quantitative real-time PCR was performed in triplicate using the PowerUp SYBR Green Master Mix. The following pre-made 5' nuclease assays were used: PI4K2A (Hs.PT.58.733616); PI4KB (Hs.PT.58.14990511); ACBD3 (Hs.PT.58.26724987); ZDHHC3 (Hs.PT.58.45384099); HPRT (Hs.PT.58v.45621572). HPRT was used as a reference to normalize PCR products.

Western blotting

Patient fibroblasts, HEK293 Cas9, and tsA201 cells were homogenized on ice in RIPA lysis buffer supplemented with complete Mini protease inhibitor cocktail. After centrifugation (20,400 *g*, 4°C, 25 min), the concentration of protein lysates in the supernatant was determined using Pierce BCA Protein Assay Kit. Protein samples were separated on 4 to 12% polyacrylamide Bis-Tris gel for 1h15 at 155V and electrophoretically blotted onto polyvinylidene difluoride membranes using a Mini-Bolt system (A25977; Thermo Fisher Scientific). After 1 h incubation at room temperature in TBS buffer supplemented with 0.05% Tween-20 (TBS–T) and 7% non-fat dry milk, membranes were exposed overnight at 4°C to the following primary antibodies in TBS-Tween-20 0.05%: mouse monoclonal β-actin, GAPDH, rabbit polyclonal PI4KIIα, rabbit polyclonal PI4KIIIβ, rabbit polyclonal OSBP, rabbit polyclonal SAC1, mouse monoclonal ACBD3. Membranes were washed in TBS-Tween-20 0.05% and incubated for 1 h at room temperature with fluorescent secondary antibodies: goat anti-rabbit 680RD and goat anti-Mouse 800CW. Signals were detected using Sapphire Gel Imager (Azure Biosystems) and quantified using ImageJ software.

Lipid mass spectrometry

Phosphoinositide levels were quantified by a refined mass spectrometry procedure, as described previously (Traynor-Kaplan *et al*, 2017; Vivas *et al*, 2019). Briefly, endogenous lipids from brain samples and internal standards were extracted with n-butanol and chloroform. After methylation-mediated derivatization, samples were subjected to a C4 column in an acetonitrile formic acid gradient. Post-column eluate was infused with sodium formate and then monitored by a Waters XEVO TQ-S MS/MS in multiple reaction monitoring mode (MRM) using electrospray and positive ion mode. Total integrated areas under peaks from sample and standard elution profiles were quantified using MassLynx software. Peak areas of individual phosphoinositide species from the biological sample were normalized to synthetic standards and further corrected for tissue amount using total protein.

Statistical analysis

Statistical analysis was performed using GraphPad Prism, version 8.4 (GraphPad Software, San Diego, California USA). All the data values are presented as means ± SEM. Number of technical and biological replicates is based on previously published observations and is consistent with the general number of replicates and conditions commonly accepted in the field. Data were assessed for normality of distribution using a D'Agostino & Pearson test and potential outliers were identified using a two-sided Grubbs' test, with an alpha value of 0.05, to determine whether values within a dataset have significant outliers. Analyses containing excluded values are noted in the figure legends. Statistical significance was determined using appropriate unpaired two-tailed Student's *t*-test, nonparametric tests (Mann–Whitney), or one-way/two-way analysis of variance (ANOVA) for multiple comparisons with appropriate *post hoc* test. $P < 0.05$ was considered statistically significant ($*P \leq 0.05$, $**P \leq 0.01$, $***P \leq 0.001$, $****P \leq 0.001$).

Data availability

Lipid mass spectrometry data produced in this study are available at MetaboLights database with the following ID: MTBLS2612 (http://www.ebi.ac.uk/metabolights/MTBLS2612).

Expanded View for this article is available online.

Acknowledgments

We thank members of the Dickson and Dixon laboratories, and Dr. Martin Kruse (Bates College) for the helpful advice and comments. We are extremely grateful to those laboratories (see Materials and methods) that shared reagents, plasmids, and cells lines used in this study. Finally, special thanks to the attendees of the Michael, Marcia, and Christa Parseghian Scientific Conference for NPC Research for their insightful comments and suggestions, which motivated several of the experiments found herein. This work was supported by an Ara Parseghian Medical Research Foundation award (E.J. Dickson); University of California funds (E.J. Dickson); and National Institutes of Health grant R01 GM127513 (E.J. Dickson); a Pharmacology National Institutes of Health T32 training award T32GM099608 (S.A. Tiscione); National Institutes of Health grants R01 NS109176 (S. Simó), R01 HL06773 (D.S. Ory), and R01 AG063796 (R.E. Dixon).

Author contributions

CK, OV, and EJD conceived, designed, and executed experiments; collected, analyzed, and interpreted data; and wrote and revised the manuscript. MC, JGJ, SAT, and SS executed experiments and revised the manuscript. RED conceived experiments, interpreted data, and revised the manuscript. DSO interpreted data and revised the manuscript. All authors approved the final version of the manuscript for publication and agree to be accountable for all aspects of the work. All listed authors meet the requirements for authorship, and all those who qualify for authorship are listed.

Conflict of interest

The authors declare that they have no conflict of interest.

References

Alvarez-Prats A, Bjelobaba I, Aldworth Z, Baba T, Abebe D, Kim YJ, Stojilkovic SS, Stopfer M, Balla T (2018) Schwann-cell-specific deletion of phosphatidylinositol 4-kinase alpha causes aberrant myelination. *Cell Rep* 23: 2881 – 2890

Antonny B, Bigay J, Mesmin B (2018) The oxysterol-binding protein cycle: burning off PI(4)P to transport cholesterol. *Annu Rev Biochem* 87: 809 – 837

Balla A, Balla T (2006) Phosphatidylinositol 4-kinases: old enzymes with emerging functions. *Trends Cell Biol* 16: 351 – 361

Balla A, Tuymetova G, Barshishat M, Geiszt M, Balla T (2002) Characterization of type II phosphatidylinositol 4-kinase isoforms reveals association of the enzymes with endosomal vesicular compartments. *J Biol Chem* 277: 20041 – 20050

Balla T (2013) Phosphoinositides: tiny lipids with giant impact on cell regulation. *Physiol Rev* 93: 1019 – 1137

Barylko B, Mao YS, Wlodarski P, Jung G, Binns DD, Sun HQ, Yin HL, Albanesi JP (2009) Palmitoylation controls the catalytic activity and subcellular distribution of phosphatidylinositol 4-kinase II{alpha}. *J Biol Chem* 284: 9994 – 10003

Bishe B, Syed GH, Field SJ, Siddiqui A (2012) Role of phosphatidylinositol 4-phosphate (PI4P) and its binding protein GOLPH3 in hepatitis C virus secretion. *J Biol Chem* 287: 27637 – 27647

Blagoveshchenskaya A, Cheong FY, Rohde HM, Glover G, Knodler A, Nicolson T, Boehmelt G, Mayinger P (2008) Integration of Golgi trafficking and growth factor signaling by the lipid phosphatase SAC1. *J Cell Biol* 180: 803 – 812

Boncompain G, Divoux S, Gareil N, de Forges H, Lescure A, Latreche L, Mercanti V, Jollivet F, Raposo G, Perez F (2012) Synchronization of secretory protein traffic in populations of cells. *Nat Methods* 9: 493 – 498

Bottanelli F, Kilian N, Ernst AM, Rivera-Molina F, Schroeder LK, Kromann EB, Lessard MD, Erdmann RS, Schepartz A, Baddeley D *et al* (2017) A novel physiological role for ARF1 in the formation of bidirectional tubules from the Golgi. *Mol Biol Cell* 28: 1676 – 1687

Brown MS, Goldstein JL (1997) The SREBP pathway: regulation of cholesterol metabolism by proteolysis of a membrane-bound transcription factor. *Cell* 89: 331 – 340

Bunney TD, Katan M (2010) Phosphoinositide signalling in cancer: beyond PI3K and PTEN. *Nat Rev Cancer* 10: 342 – 352

Burgett AWG, Poulsen TB, Wangkanont K, Anderson DR, Kikuchi C, Shimada K, Okubo S, Fortner KC, Mimaki Y, Kuroda M *et al* (2011) Natural products reveal cancer cell dependence on oxysterol-binding proteins. *Nat Chem Biol* 7: 639 – 647

Castellano BM, Thelen AM, Moldavski O, Feltes McKenna, van der Welle REN, Mydock-McGrane L, Jiang X, van Eijkeren RJ, Davis OB, Louie SM *et al* (2017) Lysosomal cholesterol activates mTORC1 via an SLC38A9–Niemann-Pick C1 signaling complex. *Science* 355: 1306 – 1311

Chalupska D, Różycki B, Humpolickova J, Faltova L, Klima M, Boura E (2019) Phosphatidylinositol 4-kinase IIIβ (PI4KB) forms highly flexible heterocomplexes that include ACBD3, 14-3-3, and Rab11 proteins. *Sci Rep* 9: 567

Condon KJ, Sabatini DM (2019) Nutrient regulation of mTORC1 at a glance. *J Cell Sci* 132: jcs222570

De Matteis MA, Godi A (2004) PI-loting membrane traffic. *Nat Cell Biol* 6: 487 – 492

Dickson EJ, Hille B (2019) Understanding phosphoinositides: rare, dynamic, and essential membrane phospholipids. *Biochem J* 476: 1 – 23

Dickson EJ, Jensen JB, Vivas O, Kruse M, Traynor-Kaplan AE, Hille B (2016) Dynamic formation of ER-PM junctions presents a lipid phosphatase to regulate phosphoinositides. *J Cell Biol* 213: 33 – 48

Dong R, Saheki Y, Swarup S, Lucast L, Harper JW, Camilli P (2016) Endosome-ER contacts control actin nucleation and retromer function through VAP-dependent regulation of PI4P. *Cell* 166: 408 – 423

Frolov A, Zielinski SE, Crowley JR, Dudley-Rucker N, Schaffer JE, Ory DS (2003) NPC1 and NPC2 regulate cellular cholesterol homeostasis through generation of low density lipoprotein cholesterol-derived oxysterols. *J Biol Chem* 278: 25517 – 25525

Fruman DA, Chiu H, Hopkins BD, Bagrodia S, Cantley LC, Abraham RT (2017) The PI3K pathway in human disease. *Cell* 170: 605 – 635

Fukata M, Fukata Y, Adesnik H, Nicoll RA, Bredt DS (2004) Identification of PSD-95 palmitoylating enzymes. *Neuron* 44: 987 – 996

Greninger AL, Knudsen GM, Betegon M, Burlingame AL, Derisi JL (2012) The 3A protein from multiple picornaviruses utilizes the golgi adaptor protein ACBD3 to recruit PI4KIIIβ. *J Virol* 86: 3605 – 3616

Greninger AL, Knudsen GM, Betegon M, Burlingame AL, DeRisi JL (2013) ACBD3 interaction with TBC1 domain 22 protein is differentially affected by enteroviral and kobuviral 3A protein binding. *MBio* 4: e00098-13

Guo J, Wenk MR, Pellegrini L, Onofri F, Benfenati F, De Camilli P (2003) Phosphatidylinositol 4-kinase type IIalpha is responsible for the phosphatidylinositol 4-kinase activity associated with synaptic vesicles. *Proc Natl Acad Sci USA* 100: 3995 – 4000

Hammond GR, Machner MP, Balla T (2014) A novel probe for phosphatidylinositol 4-phosphate reveals multiple pools beyond the Golgi. *J Cell Biol* 205: 113 – 126

Hausser A, Storz P, Martens S, Link G, Toker A, Pfizenmaier K (2005) Protein kinase D regulates vesicular transport by phosphorylating and activating phosphatidylinositol-4 kinase IIIbeta at the Golgi complex. *Nat Cell Biol* 7: 880 – 886

Haynes LP, Thomas GM, Burgoyne RD (2005) Interaction of neuronal calcium sensor-1 and ADP-ribosylation factor 1 allows bidirectional control of phosphatidylinositol 4-kinase beta and trans-Golgi network-plasma membrane traffic. *J Biol Chem* 280: 6047 – 6054

Hille B, Dickson EJ, Kruse M, Vivas O, Suh BC (2015) Phosphoinositides regulate ion channels. *Biochim Biophys Acta* 1851: 844 – 856

Houlihan LM, Christoforou A, Arbuckle MI, Torrance HS, Anderson SM, Muir WJ, Porteous DJ, Blackwood DH, Evans KL (2009) A case-control association study and family-based expression analysis of the bipolar disorder candidate gene PI4K2B. *J Psychiatr Res* 43: 1272 – 1277

Infante RE, Radhakrishnan A (2017) Continuous transport of a small fraction of plasma membrane cholesterol to endoplasmic reticulum regulates total cellular cholesterol. *Elife* 6: e25466

Jović M, Kean MJ, Szentpetery Z, Polevoy G, Gingras A-C, Brill JA, Balla T (2012) Two phosphatidylinositol 4-kinases control lysosomal delivery of the Gaucher disease enzyme, β-glucocerebrosidase. *Mol Biol Cell* 23: 1533 – 1545

Jungerius BJ, Hoogendoorn ML, Bakker SC, Van't Slot R, Bardoel AF, Ophoff RA, Wijmenga C, Kahn RS, Sinke RJ (2008) An association screen of myelin-related genes implicates the chromosome 22q11 PIK4CA gene in schizophrenia. *Mol Psychiatry* 13: 1060 – 1068

Klima M, Tóth DJ, Hexnerova R, Baumlova A, Chalupska D, Tykvart J, Rezabkova L, Sengupta N, Man P, Dubankova A *et al* (2016) Structural insights and *in vitro* reconstitution of membrane targeting and activation of human PI4KB by the ACBD3 protein. *Sci Rep* 6: 23641

Komatsu M, Waguri S, Chiba T, Murata S, Iwata J, Tanida I, Ueno T, Koike M, Uchiyama Y, Kominami E *et al* (2006) Loss of autophagy in the central nervous system causes neurodegeneration in mice. *Nature* 441: 880 – 884

Kruse M, Vivas O, Traynor-Kaplan A, Hille B (2016) Dynamics of Phosphoinositide-Dependent Signaling in Sympathetic Neurons. *J Neurosci* 36: 1386 – 1400

Leissring MA, Paul BA, Parker I, Cotman CW, LaFerla FM (1999) Alzheimer's presenilin-1 mutation potentiates inositol 1,4,5-trisphosphate-mediated calcium signaling in Xenopus oocytes. *J Neurochem* 72: 1061 – 1068

Levine TP, Munro S (2002) Targeting of Golgi-specific pleckstrin homology domains involves both PtdIns 4-kinase-dependent and -independent components. *Curr Biol* 12: 695 – 704

Lim C-Y, Davis OB, Shin HR, Zhang J, Berdan CA, Jiang X, Counihan JL, Ory DS, Nomura DK, Zoncu R (2019) ER–lysosome contacts enable cholesterol sensing by mTORC1 and drive aberrant growth signalling in Niemann-Pick type C. *Nat Cell Biol* 21: 1206 – 1218

Liscum L, Faust JR (1987) Low density lipoprotein (LDL)-mediated suppression of cholesterol synthesis and LDL uptake is defective in Niemann-Pick type C fibroblasts. *J Biol Chem* 262: 17002 – 17008

Liu X, Salokas K, Tamene F, Jiu Y, Weldatsadik RG, Öhman T, Varjosalo M (2018) An AP-MS- and BioID-compatible MAC-tag enables comprehensive mapping of protein interactions and subcellular localizations. *Nat Commun* 9: 1188

Loewen CJ, Roy A, Levine TP (2003) A conserved ER targeting motif in three families of lipid binding proteins and in Opi1p binds VAP. *Embo j* 22: 2025 – 2035

Lu D, Sun HQ, Wang H, Barylko B, Fukata Y, Fukata M, Albanesi JP, Yin HL (2012) Phosphatidylinositol 4-kinase IIα is palmitoylated by Golgi-localized palmitoyltransferases in cholesterol-dependent manner. *J Biol Chem* 287: 21856 – 21865

Lu F, Liang Q, Abi-Mosleh L, Das A, De Brabander JK, Goldstein JL, Brown MS (2015) Identification of NPC1 as the target of U18666A, an inhibitor of lysosomal cholesterol export and Ebola infection. *eLife* 4: e12177

McPhail JA, Lyoo HR, Pemberton JG, Hoffmann RM, van Elst W, Strating JR, Jenkins ML, Stariha JT, Powell CJ, Boulanger MJ *et al* (2019) Characterization of the c10orf76-PI4KB complex and its necessity for Golgi PI4P levels and enterovirus replication. *EMBO Rep* 21: e48441

Mesmin B, Bigay J, Moser von Filseck J, Lacas-Gervais S, Drin G, Antonny B (2013) A four-step cycle driven by PI(4)P hydrolysis directs sterol/PI(4)P exchange by the ER-Golgi tether OSBP. *Cell* 155: 830 – 843

Mesmin B, Bigay J, Moser von Filseck J, Lacas-Gervais S, Drin G, Antonny B (2013) A four-step cycle driven by PI(4)P hydrolysis directs Sterol/PI(4)P exchange by the ER-Golgi tether OSBP. *Cell* 155: 830 – 843

Mesmin B, Bigay J, Polidori J, Jamecna D, Lacas-Gervais S, Antonny B (2017) Sterol transfer, PI4P consumption, and control of membrane lipid order by endogenous OSBP. *EMBO J* 36: 3156 – 3174

Mesmin B, Kovacs D, D'Angelo G (2019) Lipid exchange and signaling at ER-Golgi contact sites. *Curr Opin Cell Biol* 57: 8 – 15

Millard EE, Srivastava K, Traub LM, Schaffer JE, Ory DS (2000) Niemann-pick type C1 (NPC1) overexpression alters cellular cholesterol homeostasis. *J Biol Chem* 275: 38445 – 38451

Nhek S, Ngo M, Yang X, Ng MM, Field SJ, Asara JM, Ridgway ND, Toker A (2010) Regulation of oxysterol-binding protein golgi localization through protein kinase D–mediated phosphorylation. *Mol Biol Cell* 21: 2327 – 2337

Palmer DJ, Helms JB, Beckers CJ, Orci L, Rothman JE (1993) Binding of coatomer to Golgi membranes requires ADP-ribosylation factor. *J Biol Chem* 268: 12083 – 12089

Pentchev PG, Comly ME, Kruth HS, Vanier MT, Wenger DA, Patel S, Brady RO (1985) A defect in cholesterol esterification in Niemann-Pick disease (type C) patients. *Proc Natl Acad Sci U S A* 82: 8247 – 8251

Péresse T, Kovacs D, Subra M, Bigay J, Tsai M-C, Polidori J, Gautier R, Desrat S, Fleuriot L, Debayle D *et al* (2020) Molecular and cellular dissection of the oxysterol-binding protein cycle through a fluorescent inhibitor. *J Biol Chem* 295: 4277 – 4288

Peretti D, Dahan N, Shimoni E, Hirschberg K, Lev S (2008) Coordinated lipid transfer between the endoplasmic reticulum and the Golgi complex requires the VAP proteins and is essential for Golgi-mediated transport. *Mol Biol Cell* 19: 3871 – 3884

Peterson TR, Sengupta S, Harris T, Carmack A, Kang S, Balderas E, Guertin D, Madden K, Carpenter A, Finck B *et al* (2011) mTOR complex 1 regulates Lipin 1 localization to control the SREBP pathway. *Cell* 146: 408 – 420

Praggastis M, Tortelli B, Zhang J, Fujiwara H, Sidhu R, Chacko A, Chen Z, Chung C, Lieberman AP, Sikora J *et al* (2015) A murine Niemann-Pick C1 I1061T knock-in model recapitulates the pathological features of the most prevalent human disease allele. *J Neurosci* 35: 8091 – 8106

Rawson RB, DeBose-Boyd R, Goldstein JL, Brown MS (1999) Failure to cleave sterol regulatory element-binding proteins (SREBPs) causes cholesterol auxotrophy in Chinese hamster ovary cells with genetic absence of SREBP cleavage-activating protein. *J Biol Chem* 274: 28549 – 28556

Rocha N, Kuijl C, van der Kant R, Janssen L, Houben D, Janssen H, Zwart W, Neefjes J (2009) Cholesterol sensor ORP1L contacts the ER protein VAP to control Rab7-RILP-p150 Glued and late endosome positioning. *J Cell Biol* 185: 1209 – 1225

Rome S, Lecomte V, Meugnier E, Rieusset J, Debard C, Euthine V, Vidal H, Lefai E (2008) Microarray analyses of SREBP-1a and SREBP-1c target genes identify new regulatory pathways in muscle. *Physiol Genomics* 34: 327 – 337

Sasaki J, Ishikawa K, Arita M, Taniguchi K (2012) ACBD3-mediated recruitment of PI4KB to picornavirus RNA replication sites. *EMBO J* 31: 754 – 766

Serafini T, Orci L, Amherdt M, Brunner M, Kahn RA, Rothmant JE (1991) ADP-Ribosylation factor is a subunit of the coat of Golgi-derived COP-coated vesicles: a novel role for a GTP-binding protein. *Cell* 67: 239 – 253

Simons JP, Al-Shawi R, Minogue S, Waugh MG, Wiedemann C, Evangelou S, Loesch A, Sihra TS, King R, Warner TT *et al* (2009) Loss of phosphatidylinositol 4-kinase 2alpha activity causes late onset degeneration of spinal cord axons. *Proc Natl Acad Sci U S A* 106: 11535 – 11539

Sridhar S, Patel B, Aphkhazava D, Macian F, Santambrogio L, Shields D, Cuervo AM (2013) The lipid kinase PI4KIIIbeta preserves lysosomal identity. *EMBO J* 32: 324 – 339

Staiano L, De Leo MG, Persico M, De Matteis MA (2015) Mendelian disorders of PI metabolizing enzymes. *Biochim Biophys Acta* 1851: 867 – 881

Szentpetery Z, Varnai P, Balla T (2010) Acute manipulation of Golgi phosphoinositides to assess their importance in cellular trafficking and signaling. *Proc Natl Acad Sci U S A* 107: 8225 – 8230

Thapa N, Tan X, Choi S, Lambert PF, Rapraeger AC, Anderson RA (2016) The hidden conundrum of phosphoinositide signaling in cancer. *Trends Cancer* 2: 378 – 390

Tiscione SA, Vivas O, Ginsburg KS, Bers DM, Ory DS, Santana LF, Dixon RE, Dickson EJ (2019) Disease-associated mutations in Niemann-Pick type C1 alter ER calcium signaling and neuronal plasticity. *J Cell Biol* 218: 4141 – 4156

Toth B, Balla A, Ma H, Knight ZA, Shokat KM, Balla T (2006) Phosphatidylinositol 4-kinase IIIbeta regulates the transport of ceramide between the endoplasmic reticulum and Golgi. *J Biol Chem* 281: 36369 – 36377

Traynor-Kaplan A, Kruse M, Dickson EJ, Dai G, Vivas O, Yu H, Whittington D, Hille B (2017) Fatty-acyl chain profiles of cellular phosphoinositides. *Biochim Biophys Acta* 1862: 513 – 522

Venditti R, Masone MC, Rega LR, Di Tullio G, Santoro M, Polishchuk E, Serrano IC, Olkkonen VM, Harada A, Medina DL *et al* (2019) The activity of Sac1 across ER–TGN contact sites requires the four-phosphate-adaptor-protein-1. *J Cell Biol* 218: 783 – 797

Vihervaara T, Uronen RL, Wohlfahrt G, Bjorkhem I, Ikonen E, Olkkonen VM (2011) Sterol binding by OSBP-related protein 1L regulates late endosome motility and function. *Cell Mol Life Sci* 68: 537 – 551

Vivas O, Tiscione SA, Dixon RE, Ory DS, Dickson EJ (2019) Niemann-Pick Type C disease reveals a link between lysosomal cholesterol and PtdIns(4,5)P2 that regulates neuronal excitability. *Cell Rep* 27: 2636 – 2648.e2634

Wakana Y, Hayashi K, Nemoto T, Watanabe C, Taoka M, Angulo-Capel J, Garcia-Parajo MF, Kumata H, Umemura T, Inoue H *et al* (2021) The ER cholesterol sensor SCAP promotes CARTS biogenesis at ER-Golgi membrane contact sites. *J Cell Biol* 220: e202002150

Wang YJ, Wang J, Sun HQ, Martinez M, Sun YX, Macia E, Kirchhausen T, Albanesi JP, Roth MG, Yin HL (2003) Phosphatidylinositol 4 phosphate regulates targeting of clathrin adaptor AP-1 complexes to the Golgi. *Cell* 114: 299 – 310

Waugh MG (2019) The Great Escape: how phosphatidylinositol 4-kinases and PI4P promote vesicle exit from the Golgi (and drive cancer). *Biochem J* 476: 2321 – 2346

Waugh MG, Minogue S, Anderson JS, Balinger A, Blumenkrantz D, Calnan DP, Cramer R, Hsuan JJ (2003) Localization of a highly active pool of type II phosphatidylinositol 4-kinase in a p97/valosin-containing-protein-rich fraction of the endoplasmic reticulum. *Biochem J* 373: 57 – 63

Waugh MG, Minogue S, Chotai D, Berditchevski F, Hsuan JJ (2006) Lipid and peptide control of phosphatidylinositol 4-kinase IIalpha activity on Golgi-endosomal Rafts. *J Biol Chem* 281: 3757 – 3763

Wei YJ, Sun HQ, Yamamoto M, Wlodarski P, Kunii K, Martinez M, Barylko B, Albanesi JP, Yin HL (2002) Type II phosphatidylinositol 4-kinase beta is a cytosolic and peripheral membrane protein that is recruited to the plasma membrane and activated by Rac-GTP. *J Biol Chem* 277: 46586 – 46593

Weixel KM, Blumental-Perry A, Watkins SC, Aridor M, Weisz OA (2005) Distinct Golgi populations of phosphatidylinositol 4-phosphate regulated by phosphatidylinositol 4-kinases. *J Biol Chem* 280: 10501 – 10508

White RS, Bhattacharya AK, Chen Y, Byrd M, McMullen MF, Siegel SJ, Carlson GC, Kim SF (2016) Lysosomal iron modulates NMDA receptor-mediated excitation via small GTPase, Dexras1. *Mol Brain* 9: 38

Wong K, Meyers R, Cantley LC (1997) Subcellular locations of phosphatidylinositol 4-kinase isoforms. *J Biol Chem* 272: 13236 – 13241

Zewe JP, Wills RC, Sangappa S, Goulden BD, Hammond GR (2018) SAC1 degrades its lipid substrate PtdIns4P in the endoplasmic reticulum to maintain a steep chemical gradient with donor membranes. *Elife* 7: e35588